

METALOXIDE NANOPEROVSKITES: SYNTHESIS CONDITIONS AND CHARACTERIZATION

Igor Fesych¹
Sergiy Nedilko²

DOI: <https://doi.org/10.30525/978-9934-26-531-0-7>

Abstract. Due to their unique functional properties, nanomaterials based on oxide perovskites are widely used in various industries. The unique physicochemical properties of perovskites with a general composition of ABO_3 (A = La, alkali and/or alkaline earth metal, Ag; B = Mn, Fe, Co) are caused by the electronic structure of the 3-*d* metal, the competition of low-spin, intermediate spin, and high spin states, as well as the technological conditions for obtaining compounds. The *purpose* of the paper was to investigate the relationship between the chemical composition, crystal/defective structure and properties of manganites, ferrites and cobaltates, as well as to study the influence of the nature and ratio of the starting components, heat treatment temperature, modifying additives for targeted control of the physical and chemical parameters of oxide materials and for their possible further practical application. To achieve this aim, it was necessary to synthesize a series of heterovalent substituted manganites, ferrites and cobaltates using chemical homogenization methods (sol-gel and co-precipitation); to study the thermochemical behavior of the dried precipitate or dry residue after gel combustion and to establish the optimum phase formation temperatures of the final products; to conduct phase analysis of the samples and to refine the crystallographic parameters using the Rietveld method; to calculate the size of crystallites (coherent scattering regions (CSR)) and, if possible, the microstrain of the crystal lattice by the broadening of diffraction lines using the Scherrer and Williamson-Hall methods; to study the effect of defect structure, oxygen non-stoichiometry,

¹ Candidate of Chemical Sciences (PhD), Associate Professor,
Department of Inorganic Chemistry,
Taras Shevchenko National University of Kyiv, Ukraine

² Doctor of Chemical Sciences, Professor,
Department of Inorganic Chemistry,
Taras Shevchenko National University of Kyiv, Ukraine

technological parameters of synthesis on the functional properties of perovskites and to substantiate the possible practical use of synthesized nanopowders as potential catalysts, materials with magnetocaloric effect, etc. The *methodology* of the study was based on the use of modern chemical and instrumental analysis methods to confirm the reliability of scientific statements and conclusions. The phase composition and crystallite sizes of the obtained samples were controlled by powder X-ray diffraction (PXRD). Along with PXRD, Fourier transform infrared spectroscopy (FTIR) and thermal analysis were used to study the phase formation during synthesis. The defect structure was studied by electron paramagnetic resonance (EPR). The oxygen index value was determined by iodometric titration. The *results* of experimental studies showed that by using the sol-gel method of synthesis of complex oxide samples and citric acid as a gelating agent, the optimum temperature for the formation of single-phase products depends on the nature of the transition metal and crystal structure: for manganites and ferrites with a perovskite structure, it is 500°C, whereas pure, impurity-free perovskite-like cobaltates can be obtained only above 750°C. The size of nanoparticles (CSR values) of perovskites calculated by the Scherrer method increases in linearity to the synthesis temperature. This dependence indicates that with increasing isothermal holding temperature, particle enlargement and agglomeration are observed, but even at $T = 900^\circ\text{C}$, the nanocrystallinity of the samples is preserved. The heterovalent substitution in the perovskite structure can increase the charge order in the system and leads to changes in crystallographic parameters, catalytic activity, Curie temperature, magnetic entropy, electrophysical and optical properties of these compounds. *Practical implications.* Determining the effect of the simultaneous introduction of multivalent substituents into the perovskite matrix and the temperature of isothermal holding on the properties of samples is of both theoretical and practical interest. Finding the relationship between the composition, synthesis conditions, and properties of oxide perovskites allows obtaining samples with controlled, predefined functional characteristics. *Value/originality.* The optimal conditions for the preparation of single-phase complex oxide nanopowders based on manganese, cobalt and ferrite were determined, and the regularities of the effect of the concentration of the modifying additive and the temperature of isothermal holding on the phase composition, crystallographic parameters and nanoparticle size (CSR value) of the samples were established.

Introduction

Complex oxide compounds based on 3d transition metals and REEs with perovskite and/or perovskite-like structures play an important role in the development of modern functional materials with special magnetic, electrophysical, and catalytic properties. Most of the above compounds belong to systems with strong electronic correlations (strong Coulomb repulsions between d-electrons), including lanthanum cobaltates, manganites and ferrites and their substituted analogues, which demonstrate metal-dielectric transition and exhibit high catalytic activity in the reactions of CO and hydrocarbon oxidation [1–4]. It is assumed that the band structure of such materials is attractive for the design of photocatalysts [5; 6].

The presence of transition elements in the structure of complex oxides, which can exhibit variable degrees of oxidation and be in different spin states, opens up wide opportunities for targeted variation of their physical and chemical properties. In particular, several methods of regulating the properties of complex oxide systems with perovskite structure are reported in the literature, namely: heterovalent cation substitution, creation of cation/anion vacancies, and change of synthesis temperature [7]. Along with improving the properties and developing new oxide materials, it is important to create advanced, rational technologies for their synthesis in the form of highly dispersed powders, which is one of the conditions for obtaining nanomaterials.

After the discovery of the magnetocaloric effect (MCE), the search for new materials with a large change in magnetic entropy $-\Delta S_M$ – has become relevant and a priority due to their potential application in environmentally friendly magnetic refrigerators [8; 9]. Heusler alloys, Gd-based alloys, ErCo_2 , Ho_2O_3 , etc. exhibit excellent MCE values, but most of these materials have a number of disadvantages, such as expensive starting components, complex synthesis process, large thermal and magnetic hysteresis, etc. Other potential candidates without these disadvantages, with low production cost, high chemical stability, simple preparation method and low eddy current heating are manganite-based metal oxides with high MCE values [10].

Manganites with the ABO_3 perovskite structure are good candidates for MCE. They can exhibit a significant change in magnetic entropy in weak magnetic fields near room temperature. Magnetic manganese ions in $\text{A}_{1-x}\text{A}'_x\text{MnO}_3$ manganites (A = rare earth and A' = alkali elements) can

have mixed valence ($\text{Mn}^{3+}/\text{Mn}^{4+}$) when A is non-isovalent substituted by A' ions and, as a result, different values of the spin quantum number characterising their ionic states. In addition, the charge and spin states of ions are sensitive to defects. The presence of anionic vacancies $V^{(a)}$ in the oxygen sublattice $\text{O}_{3-\Delta}$ weakens the double exchange interaction $\text{Mn}^{3+} \leftrightarrow \text{O}^{2-} \leftrightarrow \text{Mn}^{4+}$, but the change in magnetic entropy may be preserved [11]. In addition, the creation of cationic vacancies $V^{(c)}$ in the A-sublattice significantly affects the magnetotransport properties of manganites by changing the lengths of Mn-O bonds and Mn-O-Mn angles, which are also responsible for the strength of exchange interactions. This leads to the appearance of Mn^{2+} ions at the A-positions and an additional multiple ferromagnetic interaction $\text{Mn}^{3+} \leftrightarrow \text{O}^{2-} \leftrightarrow \text{Mn}^{2+} \leftrightarrow \text{O}^{2-} \leftrightarrow \text{Mn}^{4+}$ [12]. Depending on the A or A' of the deficient sublattice, the Curie temperature T_C and magnetocaloric parameters can be controlled with a very high accuracy [13]. In addition, changes in the Mn content in the A- and B-positions as a result of substitution of other ions, creation of cationic vacancies and/or introduction of superstoichiometric manganese also strongly affect the magnetotransport properties of manganites [14]. The introduction of excess Mn in the A- and/or B-positions has a several advantages: it improves the effect of magnetoresistance without reducing T_C [15]; increases the metal-dielectric phase transition temperature [16]; improves transport properties and the ferromagnetic metal state due to the appearance of Mn^{2+} ions in the A-positions, which have a half-filled conduction band; increases T_C and MCE [17].

The unique physicochemical properties of LaCoO_3 -based perovskites are due to the competition between low-spin, intermediate spin, and high spin states [18]. In ideal perovskite structures, cobalt is present in the form of diamagnetic Co^{3+} ions [19]. The introduction of alkaline earth metal ions leads to the formation of mixed-valent $\text{Co}^{3+}/\text{Co}^{4+}$ states and/or oxygen vacancies, which makes it possible to deliberately control the defectivity, electronic structure, and functional properties of cobaltates [20].

Within the various nanomaterials, perovskite-type LaFeO_3 has been widely investigated as a photocatalyst due to its high stability, electrocatalytic activity, efficient absorption of sunlight, and tunable band gap. However, the photocatalytic efficiency of LaFeO_3 is still insufficient due to the small surface area of the powder material, limited absorption of solar

energy, rapid recombination of charge carriers, and the positive level of the lower conduction band gap. In general, the effectiveness of LaFeO_3 as a photocatalyst depends on the structural features, shape, and size of the particles, so the synthesis process will have a significant impact on the target properties of lanthanum ferrite [21].

Thus, to determine the effect of (i) the concentration of cationic vacancies “□”, (ii) oxygen non-stoichiometry “ $\text{O}_{3-\Delta}$ ” and (iii) annealing temperature on the structure, morphology, valence, charge and spin states of transition metal ions in oxide perovskites, nanopowders of substituted lanthanum manganites, ferrites and cobaltates were synthesized, the optimum conditions for obtaining single-phase complex oxide nanopowders were determined, and the regularities of the effect of isothermal holding temperature on the phase composition, crystallographic parameters and nanoparticle size (CSR) of the samples were established.

1. Materials and methods of experimental studies

Currently, there is a wide range of methods for producing complex rare earth cobaltates of various sizes, from nano- to micro-size. Depending on the requirements for the physical and chemical properties of the ceramics, they are produced by solid-state methods or via chemical homogenization from solutions. For example, catalysis requires ceramics with a submicron particle size, and this is achieved by using chemical homogenization methods: co-precipitation, sol-gel method. Both ceramic and solution homogenization methods are most commonly used to produce magnetic materials, as well as ferrites and complex oxides with dielectric properties.

Synthesis methods using chemical homogenization have significant advantages over ceramic methods. Synthesis from solutions, as compared to synthesis from oxides or their solid salts, involves significantly lower annealing temperatures and ensures homogenization at the ionic and molecular level, which helps to produce materials with a high degree of homogeneity. In addition, the use of chemical homogenization methods can increase the specific surface area of complex oxides and thus improve their catalytic properties.

However, when using chemical homogenization methods from solutions, some preparative features of the synthesis should be taken into account. In particular, in some cases, co-precipitation can be problematic because of

different rates of precipitation of individual solution components. Therefore, for the method of co-precipitation of components, one of the main criteria is the choice of precipitant and the value pH of the precipitation.

Synthesis of LaCoO_3 ; Li^+ ; M^{2+} ($\text{M} = \text{Ca}, \text{Sr}, \text{Ba}$) co-doped cobaltates

A precursor synthesis method was used to obtain lanthanum cobaltates doped with alkaline-earth metal ions and lithium with perovskite structure. As precursors was used the mixture of co-precipitated hydroxooxalates of lanthanum, cobalt and alkaline-earth metals with the following composition $\text{La}_{1-3x}\text{M}_{2x}\text{Co}(\text{C}_2\text{O}_4)_{2.5-2.5x-y-z+3xy}(\text{OH})_{2y+2z-6xy} \cdot m\text{H}_2\text{O}$, where $\text{M} = \text{Ca}, \text{Sr}, \text{Ba}$; m is the number of water molecules; $0 \leq x \leq 0.05$; $0 \leq y \leq 1.5$; and $0 \leq z \leq 1.0$.

Pre-prepared aqueous solutions of lanthanum, calcium, strontium, barium, and cobalt nitrates were used as starting materials for obtaining a series of samples $\text{La}_{1-3x}\text{Li}_x\text{M}_{2x}\text{CoO}_{3+\Delta}$ ($\text{M} = \text{Ca}, \text{Sr}, \text{Ba}$; $0 \leq x \leq 0.1$) by dissolving lanthanum oxide La_2O_3 ("puriss."), calcium CaCO_3 ("p.a."), strontium SrCO_3 ("p.a."), and barium carbonates BaCO_3 ("p.a.") and cobalt (II) hydroxycarbonate $(\text{CoOH})_2\text{CO}_3$ ("puriss.") in concentrated 60% nitric acid, respectively. The acid-insoluble residue was then filtered off on a vacuum filter ($P = 0.03$ atm).

To prepare a solution of the precipitant, oxalic acid with a molar concentration of $C_M = 0.5$ mol/l, 45 g of $\text{H}_2\text{C}_2\text{O}_4$ was added to a 1 L volumetric flask and deionized water was added in portions to the marked level with vigorous mixing.

The analysis of solutions for the content of metal ions was carried out by the method of trilonometric titration: lanthanum – by direct titration with xylenol orange indicator; cobalt – by direct titration with murexide; alkaline earth metals – by reverse titration with eriochrome black T.

The initial solutions had concentrations of at least 0.5 mol/L: $\text{La}(\text{NO}_3)_3$ – 0.8 mol/l; $\text{Ca}(\text{NO}_3)_2$ – 0.7 mol/L; $\text{Sr}(\text{NO}_3)_2$ – 0.75 mol/L; $\text{Ba}(\text{NO}_3)_2$ – 0.2 mol/L (taking into account its limited solubility in water); $\text{Co}(\text{NO}_3)_2$ – 0.9 mol/L.

The synthesis of the samples in the $\text{La}_{1-3x}\text{Li}_x\text{M}_{2x}\text{CoO}_{3+\Delta}$ system ($\text{M} = \text{Ca}, \text{Sr}, \text{Ba}$; $0 \leq x \leq 0.1$) was carried out in two stages. At the first stage, a precursor was obtained by calcining a co-precipitated mixture of hydroxo-oxalates of cobalt, lanthanum, and alkaline earth metals at 750 °C for 36 hours. For this purpose, the charge of co-precipitated hydroxo-oxalates was obtained by precipitation from aqueous solutions of lanthanum, alkaline earth metal and cobalt nitrates mixed in stoichiometric proportions with $\text{H}_2\text{C}_2\text{O}_4$ solution

in accordance with Table 1. The precipitation was completed by adding portions of KOH solution ($C_M = 1$ mol/L) with visual monitoring. At the second stage, the resulting charge was ground with a stoichiometric amount of lithium carbonate Li_2CO_3 (“p.a.”) and annealed at 800°C (36 hours with intermediate grinding after 12 and 24 hours of heat treatment) to form the final product. Then the resulting mixture was homogenized, pressed into tablets at 100 MPa and kept for about 36 hours at 850°C in air.

Table 1

**Required mass and volume quantities of starting components
for sample synthesis $\text{La}_{1-3x}\text{Li}_x\text{M}_{2x}\text{CoO}_{3\pm\Delta}$ (M = Ca, Sr, Ba; $0 \leq x \leq 0,1$)
(total weight 5 g)**

Sample	Volume of solution $\text{La}(\text{NO}_3)_3$, mL	Volume of solution $\text{Ca}(\text{NO}_3)_2$, mL	Volume of solution $\text{Sr}(\text{NO}_3)_2$, mL	Volume of solution $\text{Ba}(\text{NO}_3)_2$, mL	Volume of solution $\text{Co}(\text{NO}_3)_2$, mL	Weight Li_2CO_3 , g
LaCoO_3	25.4	-	-	-	22.6	-
$\text{La}_{0,85}\text{Li}_{0,05}\text{Ca}_{0,1}\text{CoO}_3$	23	3.1	-	-	24.1	0.040
$\text{La}_{0,85}\text{Li}_{0,05}\text{Sr}_{0,1}\text{CoO}_3$	22.6	-	2.8	-	23.6	0.039
$\text{La}_{0,85}\text{Li}_{0,05}\text{Ba}_{0,1}\text{CoO}_3$	22.1	-	-	10.4	23.1	0.038

Most nanomaterials synthesis methods do not produce a final product with the required particle size (e.g., a size of less than 10 nm is important for magnetic characteristics) and high specific surface area (affecting catalytic activity). Many nanomaterials require special sophisticated equipment and significant energy costs to produce.

The combustion of reaction media formed by dissolving the initial solid chemical precursors (thermally unstable salts of organic acids, complex compounds) in water, accompanied by an exothermic redox reaction, is the basis of a new and alternative method of synthesis of nanomaterials – Solution Combustion Synthesis (SCS) [22; 23]. The composition of the solutions is determined in accordance with the principle of self-propagating high-temperature synthesis (SHS), namely, the amount of heat released during the process should be sufficient for the chemical reaction to proceed

spontaneously. The main difference between combustion in solution and 'classical' SHS is determined by the microstructure of the initial reaction medium. Whereas for SHS, mixtures of solid powders with a grain size of 1-100 μm are usually used, in solutions the reagents are mixed in the reaction mixture almost at the molecular level, and a large amount of gaseous by-products released during combustion leads, depending on the conditions of the synthesis process, to the formation of a highly dispersed target product: metal, oxide or other compound. The last, combined with energy savings and simple equipment, makes the solution combustion process particularly attractive for the development of technologies for the industrial production of various nanomaterials and their use in energy conversion and storage sources, optical devices, catalysts, and ceramics. Therefore, it is extremely important to study the physicochemical basis of the combustion process in solutions for various reaction systems, which will allow regulating the functional properties of powdered materials.

Usually, water-soluble metal nitrates are used as an oxidant, and water-soluble organic substances are used as a reductant (fuel): water-soluble linear and cyclic organic amines, acids and amino acids, etc.

Sol-gel synthesis of substituted manganites

Thus, to determine the effect of non-isovalent substitution of lanthanum by one- and/or two-charged ions and the presence of cationic vacancies " \square_x " on the structural features of lanthanum manganites, were synthesized $\text{La}_{1-x}\text{Sr}_x\text{MnO}_3$ ($0.23 \leq x \leq 0.33$), $\text{La}_{0.8-x}\square_x\text{Na}_{0.2}\text{MnO}_3$ ($0 \leq x \leq 0.05$) nanopowders.

Nanocrystalline samples of non-stoichiometric manganites $\text{La}_{0.8-x}\square_x\text{Na}_{0.2}\text{Mn}_{1+x}\text{O}_{3-\Delta}$ ($0 \leq x \leq 0.05$) were synthesized by the sol-gel autocombustion method using the following starting materials: lanthanum nitrate hexahydrate $\text{La}(\text{NO}_3)_3 \cdot 6\text{H}_2\text{O}$ (99.9% metals basis), sodium nitrate NaNO_3 (ACS, $\geq 99.0\%$), manganese (II) nitrate tetrahydrate $\text{Mn}(\text{NO}_3)_2 \cdot 4\text{H}_2\text{O}$ (98%) and citric acid $\text{C}_6\text{H}_8\text{O}_7 \cdot \text{H}_2\text{O}$ (99,995% metals). The method involves an exothermic and self-sustained thermally induced redox reaction of a xerogel obtained from an aqueous solution containing the target metal nitrates (oxidant) and organic acid (fuel, reducing agent).

To a weight of lanthanum, sodium and manganese nitrates taken in stoichiometric ratios, approximately 100 ml of deionised water was added until the salts were completely dissolved and citric acid (gelating agent) in an amount equal to the sum of moles of metals in solution. The pH of

the resulting clear solution was adjusted to 7 by adding 25 % ammonia solution, since above pH = 6, citric acid exists mainly in the form of HCit^{2-} and Cit^{3-} ions, which facilitates better complexation of metal ions. The homogeneous solution was then heated at 90-100°C for 6 hours and evaporated to form a homogeneous gel (Figure 1), which was finally dried. The dried gel was then heated on a hot plate at 200°C until the process of spontaneous combustion and combustion of the gel was initiated. The resulting brownish-black powder was placed in platinum crucibles and calcined at different temperatures (500°C, 700°C, and 900°C) for 20 hours. The samples were cooled spontaneously under conditions of heat exchange between the muffle furnace and the environment.

The nanocrystalline $\text{La}_{1-x}\text{Sr}_x\text{MnO}_3$ ($0.23 \leq x \leq 0.33$) powders were synthesized using citrate sol-gel method. The weighed stoichiometric amounts of lanthanum nitrate $\text{La}(\text{NO}_3)_3 \cdot 6\text{H}_2\text{O}$ (99.9% metals basis), strontium nitrate $\text{Sr}(\text{NO}_3)_2$ (ACS reagent, $\geq 99.0\%$), manganese nitrate $\text{Mn}(\text{NO}_3)_2 \cdot 4\text{H}_2\text{O}$ (98%), were first dissolved in 100mL deionized water and then added citric acid $\text{C}_6\text{H}_8\text{O}_7 \cdot \text{H}_2\text{O}$ (99.995% metals basis) to the above metal nitrate solution. The molar ratio of metal nitrates in solution to citric acid was taken as 1:1. The mixed solution was then heated at 85 – 90 °C on a hot plate. The solution became viscous and by sol-gel finally formed brown gel. The gel was dried overnight using an oven at 90 °C in order to remove excess water. Then the dried viscous gel is heated at 200 °C to initiate the spontaneous combustion. The self-ignited final product is ground into fine powder and then annealed in air at 950°C for 20 h in each case in an electric furnace. The three samples obtained by sol-gel technique were named as LSM023 ($\text{La}_{0.77}\text{Sr}_{0.23}\text{MnO}_3$), LSM028 ($\text{La}_{0.72}\text{Sr}_{0.28}\text{MnO}_3$) and LSM033 ($\text{La}_{0.67}\text{Sr}_{0.33}\text{MnO}_3$).

Sol-gel synthesis of lanthanum ferrite by different fuel

Commercial reagents were used as starting materials for the synthesis of lanthanum ferrite, namely D-glucose, citric acid, and ascorbic acid, the structural formulas of which are shown in Figure 2. They play the role of organic reagents that exhibit reducing properties. They play the role of organic reagents that exhibit reducing properties. Due to the presence of hydroxo groups in these compounds, they can participate in complexation with transition metal ions and lanthanides. All reagents were purified (“puriss.”).

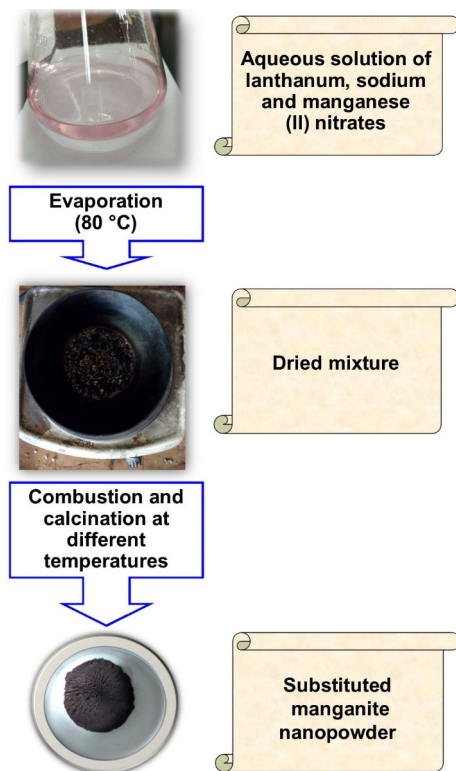


Figure 1. Scheme of substituted manganites synthesis $\text{La}_{0.8-x}\text{Na}_x\text{MnO}_3$ ($0 \leq x \leq 0.05$) by sol-gel autocombustion

For the synthesis of lanthanum ferrite, aqueous solutions of lanthanum and iron nitrates were used. The $\text{La}(\text{NO}_3)_3$ solution was obtained by dissolving lanthanum oxide, which was previously calcined in air at a temperature of $\sim 900^\circ\text{C}$, in dilute nitric acid. To prepare a solution of lanthanum nitrate with a molar concentration of about 0.7 mol/L, 120 g of oxide powder was placed in a 250 mL chemical beaker and distilled water was added in the ratio $V(\text{powder}):V(\text{water}) = 1:1$ to obtain a suspension. Then, the calculated amount of concentrated nitric acid was added dropwise according to the reaction equation

of crystalhydrate was weighed on an electronic balance to the third decimal place. The weight of crystals of iron (III) nitrate nonahydrate was quantitatively placed in a 1 L volumetric flask and brought to the mark with distilled water, and then filtered through a pleated filter from insoluble impurities. The exact concentration was determined by reverse complexometric titration in the presence of xylenol orange as an indicator and zinc nitrate as a standard solution.

The properties and particle size of ferrites synthesized by the sol-gel method depend on the type of organic chelating agent (complexing agent) and the ratio of the complexing agent to the metal salt (oxygen balance). The oxygen balance is the ratio between the complexing agent and the salts. In accordance with the principles used in fuel chemistry, the oxidizing and reducing valences of various elements are considered as follows: $V_C = 4$; $V_H = 1$; $V_O = -2$; $V_N = 0$, $V_M = 2$ or 3, etc. In this case, the total valences of the metal salts must be balanced by the total valences in the complexing agent. For example, in the case of $LaFeO_3$, when using metal nitrates $La(NO_3)_3$, $Fe(NO_3)_3$ and citric acid, the total valences are -15, -15 and +18, respectively.

Thus, given the stoichiometric composition of ferrite, it is necessary that $-30 + 18n = 0$ or $n = 1.67$ mol of citric acid. For example, to obtain $LaFeO_3$, the reagents $La(NO_3)_3$, $Fe(NO_3)_3$, and citric acid should be mixed in a molar ratio of 1:1:1.67. The total valences for ascorbic acid are +20 and for glucose +24.

Adjusting the ratio of the complexing agent to metal nitrate allows controlling the flame time and its effect on phase formation and growth, as well as the state of particle agglomeration (Figure 3).

It was found that with an increase in the excess of complexing agent in the gels, the combustion reaction requires oxygen supply from the outside, which leads to a decrease in the reaction rate and temperature. In addition, with an increase in the amount of complexing agent, a larger volume of gases is formed, and the heat of the reaction can be removed to the system by convection. This will reduce the likelihood of particles contacting, growing and sintering with each other, which can lead to a powder with a high specific surface area.



Figure 3. Combustion reaction of a nitrate-citrate precursor

At the same time, due to the lower reaction rate and temperature, particles with lower crystallinity and phase purity are formed. With an insufficient amount of complexing agent, the heat generated is insufficient due to the lack of reducing agent in the system, and hence the reaction rate and temperature are also reduced, resulting in a smaller particle size and increased specific surface area. Compared to systems with an excess of complexing agent, a lower carbon content in the final product can be observed. From this point of view, it is more suitable for modifying the method when the goal is to produce smaller particles.

In our work, the amount of organic complexing agents was calculated assuming an oxygen balance of zero.

Synthesis of Ag substituted manganites via pyrolysis of nitrates

During the synthesis of single-phase nanopowders of silver-containing lanthanum manganites, the use of reducing agents is unacceptable, i.e. it is impossible to obtain a pure sample without impurities of metallic silver. The latter is formed in the presence of, for example, citric acid, which is used as a fuel in the sol-gel method of autocombustion.

Therefore, the nanocrystalline $\text{La}_{0.7}\text{Ag}_{0.2}\text{Mn}_{1.1}\text{O}_3$ powder was synthesized by nitrate pyrolysis method using two different lab equipment: porcelain cup and chemical glass beaker. The weighed stoichiometric amounts of lanthanum nitrate $\text{La}(\text{NO}_3)_3 \cdot 6\text{H}_2\text{O}$ (99.9% metals basis), silver nitrate AgNO_3 (ACS reagent, $\geq 99.0\%$), manganese nitrate $\text{Mn}(\text{NO}_3)_2 \cdot 4\text{H}_2\text{O}$ (98%), were first dissolved in 100mL deionized water with constant stirring to obtain a metal nitrate solution. The mixed solution was then taken into a

porcelain cup and evaporated at 100 – 105 °C on a hot plate to remove the water molecules. The pyrolysis of the resulting viscous mixture of lanthanum, silver and manganese nitrates was carried out at 600 °C and was accompanied by the evolution of brown NO₂ gas. The obtained black powder was ground in an agate mortar, placed in alumina crucibles, and calcined at 900°C for 20 hours (sample LAM900). After repeated grinding, the substituted lanthanum manganite was heated at 1000°C with isothermal hold time 5 hours (sample LAM1000). According to another method, metal nitrate solutions were placed in a chemical glass beaker and evaporated until a grey-black solid residue was formed (Figure 4).



Figure 4. Dry residue after nitrate pyrolysis

The solid residue was then ground in an agate mortar, placed in a porcelain crucible and calcined at 750 °C for 10 hours (sample LAM700) and 800 °C for 30 hours (sample LAM800).

Synthesis nonstoichiometric La_{0.6}Sr_{0.3}Mn_{1.1}O₃ manganite

The La_{0.6}Sr_{0.3}Mn_{1.1}O₃ (LSMO) nanopowder was obtained by atomization hydrolysis method, which is analogous to the coprecipitation method, but with ultrasonic spraying of a stoichiometric mixture of component solutions over the precipitant solution at the initial synthesis stage. During the synthesis of LSMO nanopowder, La(NO₃)₃·xH₂O (99.9% metals basis), Sr(NO₃)₂ (ACS reagent, ≥99.0%), and Mn(NO₃)₂·4H₂O (purum p.a., ≥97.0%) were used

to prepare a stoichiometric mixture of components and $(\text{NH}_4)_2\text{CO}_3$ (ACS reagent, $\geq 30.0\%$ NH_3 basis) + NH_4OH (puriss. p.a., $\geq 25\%$ NH_3 basis) as a complex precipitant solution. An additional homogenization process using ultrasonic atomization ensures that most of the undesirable NH_4NO_3 is volatilized during precipitation and reduces the washing time, as well as makes it possible to obtain an ultrafine nanomaterial with a smaller particle size of ~ 20 nm compared to a size of ~ 50 – 200 nm in the co-precipitation method under the same synthesis conditions. The suspension obtained after precipitation was stirred and poured into a nutsche filter dryer for washing and squeezing out the solid phase. After extracting, the paste was dried at 200 °C (5 h) and heat treated in the air to complete crystallization. The heat treatment was carried out at 650 °C (10 h) in slow heating and cooling mode.

Modern experimental methods were used to study intermediate and final products, namely:

Powder X-Ray diffraction (PXRD). X-ray diffraction studies were carried out at room temperature using a LabX XRD-6000 diffractometer (Shimadzu, Japan) with $\text{CuK}\alpha$ radiation ($\lambda_{\text{Cu}} = 1.5406$ Å). The diffraction spectrum was acquired using the θ - 2θ scanning scheme with Bragg-Brentano focusing in the range of 2θ angles from 30 to 40° with a step $\Delta(2\theta) = 0.02^\circ$. The exposure time at each point was 1 second. The measurements were performed at a tube voltage of 35 kV and a current of 30 mA. To identify the crystallographic phases in the studied system was also used Match software (version 1.8a) and database of the International Committee for Powder Diffraction Standards (JCPDS PDF-2).

The X-ray diffraction patterns were processed by Rietveld method using the Match3 computer program with the embedded open crystallographic database COD (Crystallography Open Database – <http://www.crystallography.net/cod/> - 512 072 maps) and the FullProf Suite Program (version July 2017).

The average size D of coherent scattering regions (CSRs) in perovskite nanopowders was determined from the broadening of diffraction reflections. In the first approximation, the size of CSRs was considered as the average size of powder particles.

To confirm the nanocrystalline structure, we analyzed the diffraction data using the Scherrer and Williamson Hall methods. Using the X-ray

diffraction peak broadening method and the *Scherrer formula* [24], the crystallite size of oxide powders was calculated as follows:

$$D_s = \frac{K \cdot \lambda}{\beta_{hkl} \cdot \cos\theta_{hkl}}, \quad (1)$$

where D_s in nm is the average crystallite size along the direction normal to the diffraction plane (hkl), K is the shape factor equal to 0.9, λ is the X-ray wavelength 0.15406 nm of $\text{Cu}_{K\alpha}$ -radiation, β_{hkl} is the integral breadth of the peak related to the diffraction plane (hkl), and θ_{hkl} is the Bragg angle in radians for the crystallographic plane (hkl).

The Scherrer equation is a widely used tool to determine the crystallite size of polycrystalline samples. It was noticed that the well-known Scherrer formula was derived for a monodisperse powder with a Gaussian distribution of cubic shaped crystallite sizes.

The width of a peak profile can be described by different parameters. Most commonly, the full width at half maximum (*FWHM*) or the integral breadth (β) are used to express peak width. The *FWHM* is colloquially also known as “half width” and describes the width of a peak at half of its height. The integral breadth is defined as the integral (= area) of a peak divided by the peak height. Alternatively, you can imagine it as the width of a rectangle which has both the same area and height as the peak.

The work [24] interpreted the constant K as a relating factor between the *FWHM* and β of the Gaussian function: $FWHM = 2\sqrt{\frac{\ln 2}{\pi}} \cdot \beta = K \cdot \beta$,

suggesting that Scherrer supposed the diffraction peak to be approximated by the Gaussian, consequently, $\beta = FWHM$. Then, the Scherrer formula

may be written as $FWHM = K \frac{\lambda}{D \cdot \cos\theta}$, where $K = 2\sqrt{\frac{\ln 2}{\pi}} \approx 1$. The

constant of proportionality, K (the Scherrer constant) depends on the how the width is determined, the shape of the crystal, and the size distribution (0.94 for spherical crystals with cubic symmetry; 0.89 for integral breadth of spherical crystals without cubic symmetry) [25]. The Scherrer constant K sometimes is rounded up to 0.9.

The true integral peak width was calculated using formula:

$$\beta_{hkl} = (\beta_{exp}^2 - \beta_0^2)^{0.5} \quad (2)$$

where β_{exp} is the experimental peak width of the sample at half maximum intensity; β_0 is the instrumental broadening of the diffraction line, which depends on the design features of the diffractometer. Based on Rietveld refinement of powder X-ray diffraction patterns showed that the integral breadth of the Bragg reflections in the interval 5-30° is described by the pseudo-Voigt function with a large (up to 90% or more) contribution of the Lorentz function ($\eta \rightarrow 1$). Therefore, the Lorentz function was chosen to describe the shape of the diffraction peaks. In order to exclude the instrumental broadening β_0 , a standard silicon Si X-ray powder diffraction data is recorded under the same condition and is eliminated from the observed peak width $\beta = \beta_{exp} - \beta_0$.

Williamson-Hall method. The broadening of the reflexes in the diffractograms depends on the size of the coherently scattered regions (size broadening β_D) and the microstrain of the crystal lattice caused by defects in the crystal structure, deformations, and displacements of atoms due to the presence of dislocations (strain broadening β_ϵ). Strain-induced broadening arising from crystal defects and distortion are calculated employing Stokes-Wilson equation:

$$\epsilon = \frac{\beta^2}{4 \tan^2 \theta_{hkl}} \quad (3)$$

If the shape of diffraction reflection is described by the Lorentz function, the true integral width is defined as the sum of the size and strain broadening i.e., $\beta_{hkl} = \beta_D + \beta_\epsilon$.

The theta dependences of the size and strain broadening in the W-H analysis are described by the following equations:

$$\beta_{hkl} = \beta_D + \beta_\epsilon = \frac{K \cdot \lambda}{D_{hkl} \cdot \cos \theta_{hkl}} + 4 \mu \tan \theta_{hkl} \quad (4)$$

$$\beta_{hkl} \cdot \cos \theta_{hkl} = \frac{K \cdot \lambda}{D_{hkl}} + 4 \mu \sin \theta_{hkl} \quad (5)$$

where D_{hkl} (nm) is the average size of crystallites along the direction normal to the diffraction plane (hkl), ϵ is the strain, K is the shape factor

equal to 0.9, λ is the x-ray wavelength 0.15406 nm of $\text{Cu}_{K\alpha}$ radiation, β_{hkl} is the integral breadth of the peak related to the diffraction plane (hkl) and θ_{hkl} is the Bragg angle in radians for the crystallographic plane (hkl). From the XRD data, β_{hkl} was obtained by Lorentzian peak fit.

The $\beta_{hkl} \cdot \cos\theta_{hkl}$ term was plotted against $4\sin\theta_{hkl}$ for the perovskite samples. After performing linear approximation of the data points, it was estimated the average crystallite size from the y -intercept ($K\lambda/D_{hkl}$) and lattice strain from the slope (ε).

Calculation of the X-ray density ρ_{XRD} of the samples was carried out according to the formula:

$$\rho_{XRD} = \frac{Z \cdot M_r}{V \cdot N_A}, \quad (6)$$

where Z is the number of formula units per unit cell; M_r is the molecular weight of substituted lanthanum manganite ($\text{g}\cdot\text{mol}^{-1}$); V is the unit cell volume (cm^3); N_A is the Avogadro's number ($6.022 \cdot 10^{23} \text{ mol}^{-1}$).

The dislocation density (δ), which represents the number of defects in the sample is defined as the length of dislocation lines per unit volume of the crystal and is calculated using the equation:

$$\delta = \frac{1}{D_s^2}, \quad (7)$$

where, D_s is the crystallite size obtained from Scherrer method.

Thermogravimetry and differential thermal (TG/DTA) analysis.

The thermal behavior of the precursor powder mixture was studied by simultaneous thermogravimetric and differential thermal analysis using a DTG-60H analyzer (Shimadzu, Japan). The TG/DTA curves were carried out from room temperature to 800 °C with a heating rate of 10 °C min^{-1} . The powdered sample with mass about 1-2 mg was placed to alumina crucibles. The experiments were carried out in air at a flow rate of 100 mL min^{-1} . The reference substance was pure $\alpha\text{-Al}_2\text{O}_3$.

FTIR spectroscopy. The infrared spectra of the powders were recorded in the range of 400-4000 cm^{-1} using a Fourier transform infrared spectrophotometer Spectrum BX FT-IR (Perkin Elmer, USA). A weight of the powder under study was mixed with KBr of "puriss. spec." qualification in a proportion of 1/100 (by weight) and pressed into translucent tablets

using a hand press. The IR spectra were recorded with a resolution of 2 cm⁻¹ and signal accumulation of 32 scans.

Diffuse reflectance spectroscopy. Diffuse reflectance spectrum (DRS) of the perovskites recorded using a UV-Visible spectrophotometer UV-2600 (Shimadzu, Japan) in the wavelength range of 200 to 800 nm to estimate their band gap energy. Barium sulfate BaSO₄ used as a non-absorbing reference.

The Kubelka-Munk equation was used to theoretically describe the diffuse reflection of a powder sample:

$$F(R) = \frac{\alpha}{S} = \frac{(1-R)^2}{2R}, \quad (8)$$

where $F(R)$ is the Kubelka-Munk function; R is the reflection coefficient at a certain wavelength; α is the linear absorption coefficient, and S is the linear scattering coefficient of ferrite. The last (S) is constant when the sample thickness is much larger than the size of a single crystallite.

The value of the band gap E_g was determined using the Tauc method, which is based on the ratio:

$$(\alpha \cdot h\nu)^{1/n} = A \cdot (h\nu - E_g), \quad (9)$$

h is the Planck's constant, ν is the photon frequency, A is a constant, E_g is the energy corresponding to the width of the band gap, and n is an index that depends on the type of electronic transition: $n = 1/2$ for a direct allowed transition, $n = 3/2$ for a direct forbidden transition, $n = 2$ for an indirect allowed transition, and $n = 3$ for an indirect forbidden transition.

If we substitute $F(R)$ for α in Equation 9, we get the following equation:

$$(F(R) \cdot h\nu)^{1/n} = A \cdot (h\nu - E_g), \quad (10)$$

where $F(R)$ is the Kubelka-Munk function; R is the reflection coefficient at a certain wavelength.

The value of the energy of the optical bandgap for a commercial ferrosphenel was determined from the graphical dependence $(F(R) \cdot h\nu)^{1/n} = f(h\nu)$, where $n = 1/2$, extrapolating the straight line to $(F(R) \cdot h\nu)^2 = 0$, where the desired E_g is the point of intersection with the abscissa axis.

EPR spectroscopy. EPR spectra of polycrystalline samples were recorded at room temperature on a Bruker Elexsys E580 spectrometer.

The experimental parameters were microwave power 2 mW, radiation frequency ~ 9.9 GHz, modulation intensity 2 G, modulation frequency 100 kHz, scan time 300 s, and 1024 points. Spectra were processed using the Bruker WINEPR program. The concentration of paramagnetic centers was determined by comparing integrated intensities of spectra of synthesized and standard ($\text{CuSO}_4 \cdot 5\text{H}_2\text{O}$) samples.

Electron microscopy. The morphology and size of the particles were determined using a JEM-2200FS transmission electron microscope. High-resolution transmission electron microscopy with an accelerating voltage of 200 kV was used to obtain information on particle size and shape, as well as to determine the average interplanar distance using Gatan Microscopy Suite software based on the fast Fourier transform. Samples for TEM analysis were prepared by placing a drop of a dilute mixture of particles and acetone on a carbon-coated copper mesh. The average particle size d was obtained from the analysis of TEM images by fitting the experimental values of d with different distribution functions. The particle size d was measured using Nano Measure 1.2.5 software. It should also be noted that obtaining clear TEM images was quite difficult due to the magnetic attraction between nanoparticles and their agglomeration, since manganite nanopowder has a Curie temperature that is higher than room temperature.

Electrophysical properties. The temperature dependence of the specific electrical resistance $\rho(T)$ in the range 77-300 K was measured by the standard four-probe method on a Pillar-1UM apparatus. Pellets for resistance studies were pressed at 100 atm and were disks of diameter 15 mm and thickness 2.0-2.5 mm.

The values of the oxygen index and the average oxidation degree of transition metal in complex oxides with a perovskite structure were determined by iodometric titration. A sample of $\text{La}_{1-3x}\text{Li}_x\text{M}_{2x}\text{CoO}_{3-\Delta}$ ($M = \text{Ca}, \text{Sr}, \text{Ba}; 0 \leq x \leq 0.1$) $m = 0.05$ mg was placed in a flask, then 10 ml of HCl solution ($C_M = 0.7$ mol/L) and 10 ml of KI solution ($C_M = 1$ mol/L) were added. The sample dissolution process lasted on average from 10 to 30 minutes. The iodine formed after the dissolution of the substituted cobaltate powder was titrated with $\text{Na}_2\text{S}_2\text{O}_3$ solution ($C_M = 0.1$ mol/L) using a freshly prepared starch solution as an indicator. The error in determining the oxygen content by iodometric titration is ± 0.02 .

It is known that KI can be oxidized in the light in the presence of atmospheric oxygen according to the scheme:



To minimize iodine losses, a so-called “control experiment” (without a sample) was conducted.

The oxygen index, as well as the average degree of oxidation of the transition metal (in this case, cobalt), was determined in air at room temperature. For complex oxides with a perovskite structure (type ABO_3), partial substitution in positions A and/or B can lead to a change in the oxidation state of the transition metal and/or the formation of oxygen vacancies.

The value of the oxygen index ($3-\Delta$) was calculated by the formula:

$$3 - \Delta = 2.5 - 2 \cdot x + \frac{0.001 \cdot N \cdot (V_s - V_0) \cdot M_r}{2 \cdot m - 0.016 \cdot N \cdot (V_s - V_0)} \quad (11)$$

where C_M , V_s , and V_0 are the concentration (mol/L) and volume (ml) of $\text{Na}_2\text{S}_2\text{O}_3$ solution used for sample titration and in the “control experiment”, respectively;

M_r is the molecular weight of the reduced form of the sample $\text{La}_{1-x}\text{A}_x\text{B}^{2+}\text{O}_{3-\Delta}$ (A – alkali, alkaline earth metal; B – manganese, iron, cobalt) (g/mol).

2. Phase formation processes in oxide perovskites

Perovskite manganites. According to the phase analysis carried out by processing the powder X-ray diffraction data, it was found that after the combustion process of the nitrate-citrate gel, a mixture consisting of $\text{La}_2\text{O}_2\text{CO}_3$, Mn_3O_4 , and NaNO_2 is formed (Figure 5). The reflexes of standard monoclinic lanthanum carbonate $\text{La}_2\text{O}_2\text{CO}_3$ (JCPDS card No. 00-048-1113) are marked with blue strokes, tetragonal manganese oxide Mn_3O_4 (JCPDS card No. 00-024-0734) with green strokes, and orthorhombic sodium nitrite NaNO_2 (JCPDS card No. 00-006-0392) with red strokes.

In general, the combustion process of a nitrate-citrate gel can be considered a thermally induced redox reaction in which citrate ions act as a reducing agent and nitrate ions act as an oxidizing agent. Due to the presence of NO_3^- ions, which provide decomposition of organic components, the

reaction speed increases. As a result, sufficient energy is released to form single-phase perovskite at fairly low temperatures (even at 500 °C).

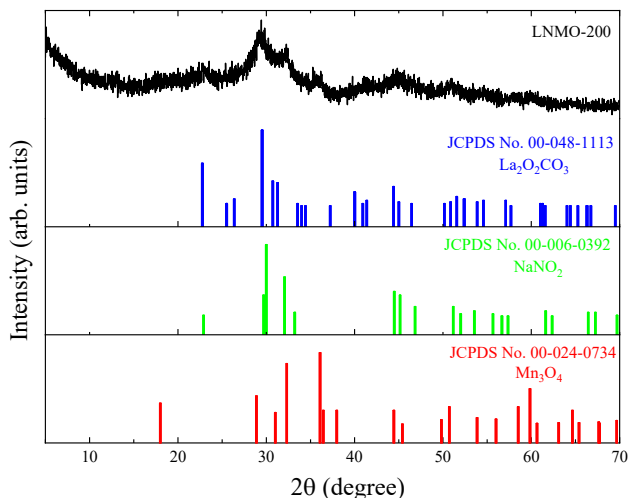


Figure 5. XRD pattern for the as-prepared $\text{La}_{0.8}\text{Na}_{0.2}\text{MnO}_3$ powder obtained after self-ignition at 200 °C. The standard reflexes of monoclinic lanthanum carbonate $\text{La}_2\text{O}_2\text{CO}_3$ (JCPDS Card No. 00-048-1113), orthorhombic sodium nitrite NaNO_2 (JCPDS Card No. 00-006-0392), and tetragonal manganese oxide Mn_3O_4 (JCPDS Card No. 00-024-0734) are also noted

The XRD data show that the dried gel after the combustion process initiated at 200 °C is a mixture of $\text{La}_2\text{O}_2\text{CO}_3$, Mn_3O_4 , and NaNO_2 phases. Simultaneous differential thermal analysis and thermogravimetry were performed to determine the changes that occurs with this mixture during further heat treatment and to determine the optimal conditions for obtaining a single-phase product.

The derivatogram of the powder mixture of La–Na–Mn–O nitrate-citrate gel after self-ignition at 200 °C can be conditionally divided into three temperature regions (see Figure 6): (i) thermal process from room temperature to 210 °C associated with slight weight loss (-4.0 %) which is

a result of evaporation of physically adsorbed water and surface hydroxyl groups removal from the combusted gel; (ii) the second significant weight loss (-13.0 %) occurs in the temperature range between 210-500 °C and can be attributed to the decomposition of *lanthanum oxycarbonate* $\text{La}_2\text{O}_2\text{CO}_3$ and sodium nitrite NaNO_2 , the presence of which in the self-ignited powder composition is confirmed by the XRD data along with the presence of manganese oxide Mn_3O_4 (see Figure 6); (iii) after 500 °C, the TG curve shows a slight mass loss (-3.3 %) and then an insignificant increase in the mass of the sample (+2.0 %), which may be associated with the implementation of redox processes in the oxide matrix with the formation of different oxidation states of manganese ions [26; 27]. Additionally, the changing mass of the sample is accompanied by a broad endo-effect. Considering the obtained thermal results, the substituted manganite synthesis was performed at 500, 700, and 900 °C to define the effect of heat treatment temperature on their functional properties.

Perovskite ferrite. According to the results of X-ray phase analysis, all synthesized samples were found to be single-phase, except for lanthanum ferrite synthesized using ascorbic acid LaFO_500_AA and glucose LaFO_500_G and calcined at 500°C (Figs. 7 and 8).

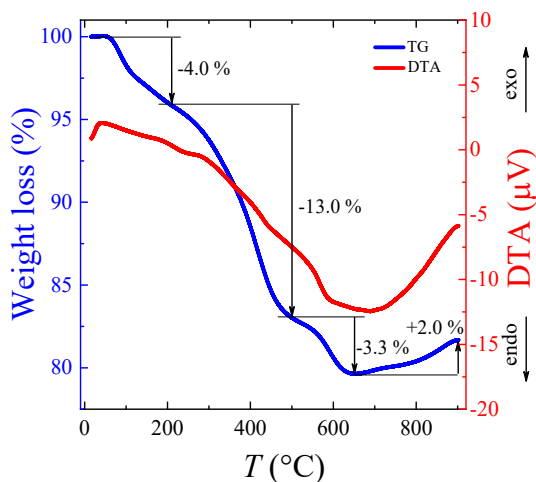


Figure 6. TG/DTA curves of the La–Na–Mn–O self-ignited powder

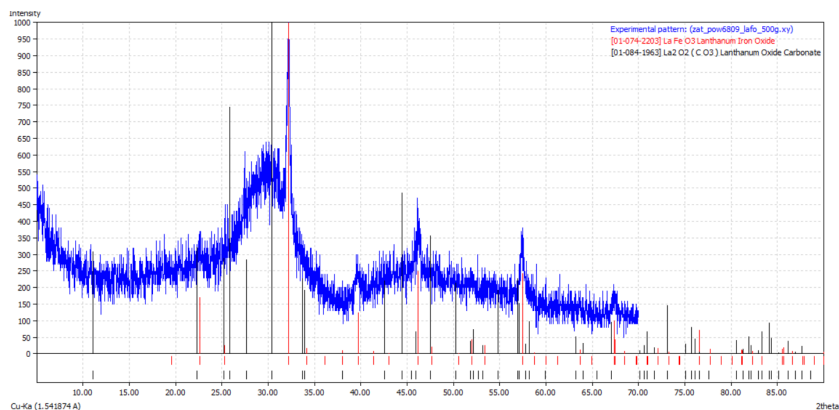


Figure 7. Phase analysis of a LaFeO_3 sample prepared with glucose and calcined at 500°C

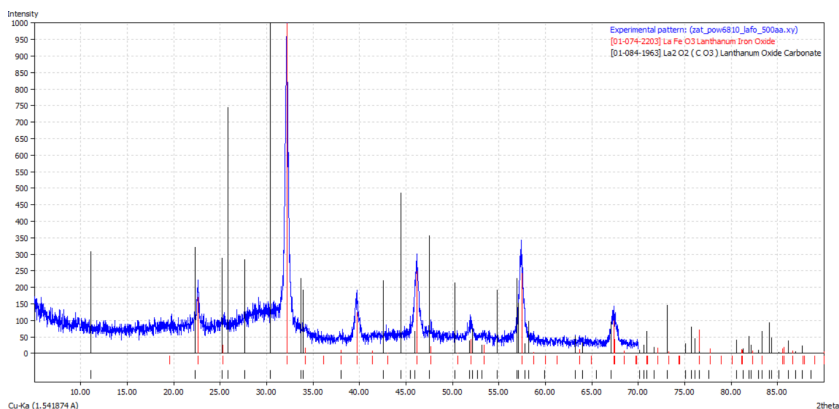


Figure 8. Phase analysis of a LaFeO_3 sample prepared with ascorbic acid and calcined at 500°C

In generally, these samples can be considered amorphous, despite the fact that the diffractograms show rather narrow peaks belonging to lanthanum ferrite (red lines in the figures). The reason for the X-ray amorphous nature of the samples is the presence of lanthanum oxocarbonate $\text{La}_2\text{O}_2(\text{CO}_3)$

(black lines in the figures), which is also confirmed by FTIR spectroscopy.

The degree of crystallinity of the samples subjected to heat treatment at 500°C increases in the order LaFO_500_G < LaFO_500_AA < LaFO_500_CA (Figure 7-9). This sequence is completely predictable, given that the combustion temperature of the nitrate-citrate gel is much higher than in the presence of ascorbic acid and glucose. The thermal energy released during the combustion process is sufficient to form a single-phase product with a high degree of crystallinity.

With an increase in the synthesis temperature, an increase in the degree of crystallinity and a decrease in the width of the reflexes on the diffractograms are observed, which is directly related to the enlargement of ferrite particles during high-temperature treatment.

The lanthanum ferrite obtained at 700°C and 900°C, regardless of the involved organic precursor, is a single-phase product that crystallizes in orthorhombic syngonation with the Pbnm space group (#62). The crystal lattice parameters are $a = 5.5635 \pm 0.0002 \text{ \AA}$, $b = 7.8532 \pm 0.0005 \text{ \AA}$, $c = 5.5543 \pm 0.0003 \text{ \AA}$, and the unit cell volume is $V = 242.68 \pm 0.02 \text{ \AA}^3$. A typical diffraction pattern for lanthanum ferrite is shown in Figure 10.

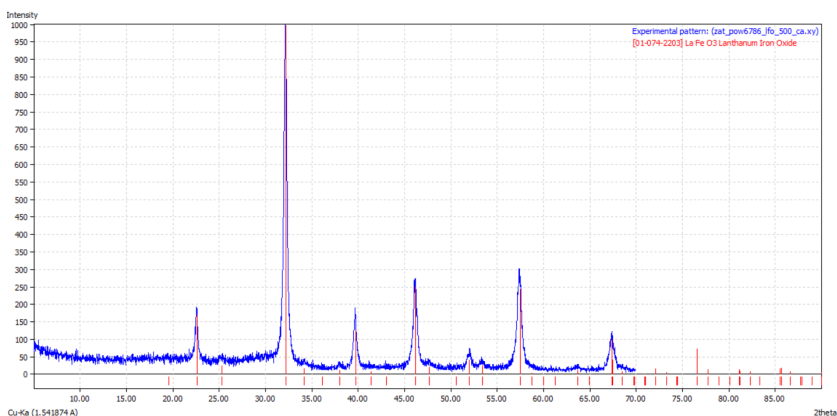


Figure 9. Phase analysis of a LaFeO₃ sample prepared with citric acid and calcined at 500°C

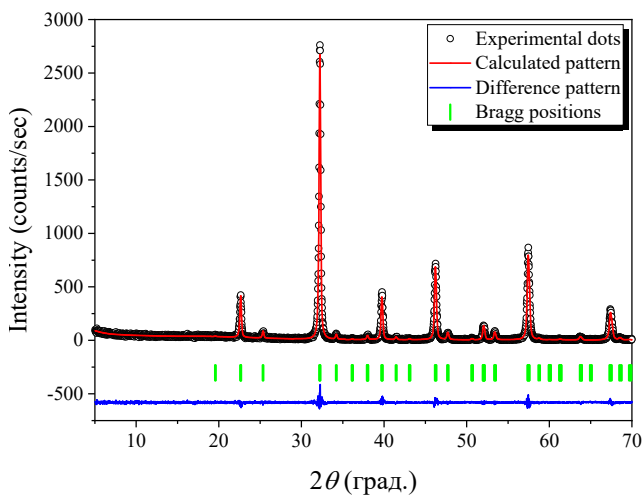


Figure 10. Typical diffractogram of lanthanum ferrite refined by Rietveld method

To study the processes occurring in the powder after the gel combustion, isothermal holding was carried out at different temperatures of 500°C, 700°C and 900°C. The duration of the temperature treatment was also the same for all samples, namely 200 minutes. The FTIR spectra of lanthanum ferrite synthesized using citric acid at 500°C, 700°C and 900°C are shown in Figure 11.

To confirm the structural information obtained by X-ray diffraction analysis, IR spectra of LaFeO_3 nanoparticles were recorded. Some specific modes of the IR spectra are shown in Figure 11. The vibrational range of the metal-oxygen (M-O) bond at approximately 400-600 cm^{-1} indicates the formation of a typical perovskite (ABO_3) structure. These results are in good agreement with previously published IR spectra for undoped LaFeO_3 .

The absorption band at approximately 400-500 cm^{-1} corresponds to asymmetric stretching and bending vibrations of the Fe-O-Fe bond, corresponding to the deformation of the FeO_6 octahedra and the change in the Fe-O-Fe bond angle, respectively. The bands at frequencies of approximately 500-600 cm^{-1} are identified as Fe-O stretching vibrations associated with the change in the Fe-O bond length.

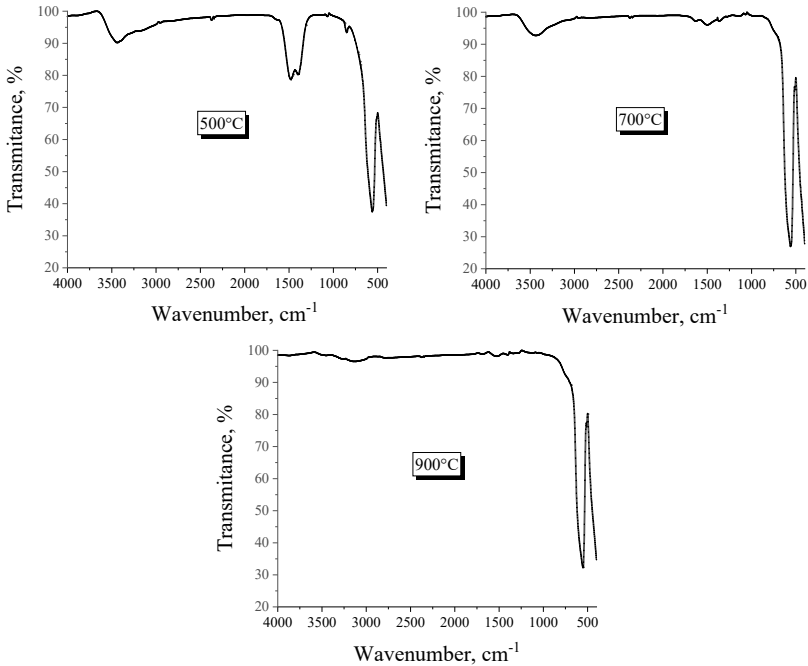


Figure 11. FTIR spectra of lanthanum ferrite obtained in the presence of citric acid for 200 minutes at different temperatures

Oxides with a perovskite structure, especially those containing iron, have a large number of active surface states, the concentration of which increases with small particle sizes. Therefore, it can be expected that the surface will absorb organic compounds formed as a result of the addition of organic precursors. Figure 11 compares the FTIR spectra of powders processed at different temperatures. The absorption bands of the FTIR spectra at different wavenumbers are marked. The absorption band at 557 cm^{-1} is characteristic of rare-earth orthoferrites and corresponds to the stretching vibrations of the Fe-O bond. A number of bands appearing in the region between 600 cm^{-1} and 1700 cm^{-1} are characteristic only for the sample calcined at 500°C . New bands appear in the spectrum at 849 cm^{-1} , 1061 cm^{-1} , 1397 cm^{-1} and 1472 cm^{-1} . The appearance of these bands

was also observed in LaFeO_3 obtained by other methods using organic precursors. The broad and intense bands at 1397 cm^{-1} and 1472 cm^{-1} and the relatively weaker bands at 1061 cm^{-1} and 849 cm^{-1} can be attributed to the fundamental vibrations of the CO_3^{2-} group and are very similar to those observed in lanthanum carbonate $\text{La}_2\text{O}_2\text{CO}_3$. The presence of bands in the region of $3200\text{--}3600\text{ cm}^{-1}$ indicates the presence of adsorbed water molecules in the samples. However, it is worth noting that the intensity of the bands corresponding to carbonates and water molecules decreases with increasing ferrite annealing temperature, and at 900°C for LaFeO_3 no oscillations other than M-O were recorded. These results are consistent with the data of X-ray phase analysis.

The absence of carbonates in the X-ray diffraction patterns indicates that these carbonates are amorphous. Let us now turn to the effect of heat treatment temperature on these combustion products. The X-ray diffraction results show that the crystallinity of the powder increases sharply for LaFO-700 and LaFO-900. It can be assumed that the high content of residual carbonates present in the burned powder and LaFO-500 prevents the increase in crystallinity. However, the intensive decomposition of these residual products in LaFO-700 is accompanied by a sharp increase in crystallinity.

The FTIR spectra of calcined LaFeO_3 precursors obtained by various methods were measured in the frequency range $700\text{--}300\text{ cm}^{-1}$ and are shown in Figure 11. Two broad absorption peaks at approximately 560 and 340 cm^{-1} were detected, which are characteristic bands of orthorhombic LaFeO_3 . The band at approximately 560 cm^{-1} (ν_1) can be attributed to the Fe-O stretching vibrations characteristic of the octahedral FeO₆ groups, while the band at approximately 340 cm^{-1} (ν_2) is due to the Fe-O-Fe deformation vibrations. The slight shifts in the band positions can be correlated with the observed slight changes in the calculated lattice parameters.

Perovskite cobaltates. The study of the co-precipitated hydroxy-oxalates charge during heat treatment was carried out using X-ray diffraction and FTIR spectroscopy methods. Figure 12 shows the evolution of the diffraction pattern of the Ca-containing complex oxide with $x = 0.05$ depending on the calcination temperature. In the X-ray diffraction pattern of the sample aged at 400°C , the signal/background ratio is very small and therefore it is not possible to clearly distinguish and assign peaks. According to the FTIR spectroscopy data (Figure 13), it can be concluded

that X-ray amorphousness is associated with the presence of water molecules (a broad band of stretching vibrations of the O – H bond in the region of 2800 – 3600 cm^{-1}).

After calcination of the charge at 400°C, a mixture of three phases is formed: cobalt oxide Co_3O_4 (★), calcium carbonate CaCO_3 (◆) and lanthanum dioxocarbonate $\text{La}_2\text{O}_2\text{CO}_3$ (▼) (in the FTIR spectrum, it corresponds to the vibration band of carbonate groups in the region of 1300–1500 cm^{-1}). The perovskite phase (▲) begins to form at 600°C, as evidenced by the presence of corresponding reflexes in the X-ray diffraction pattern. At a temperature of 700°C, the intensity of the peaks corresponding to the perovskite phase increases, but impurities of lanthanum oxide La_2O_3 (●) and cobalt Co_3O_4 (★), as well as calcium cobaltate $\text{Ca}_3\text{Co}_4\text{O}_9$ (■), are still present. The formation of a single-phase perovskite precursor was recorded after heat treatment of the charge at 750°C.

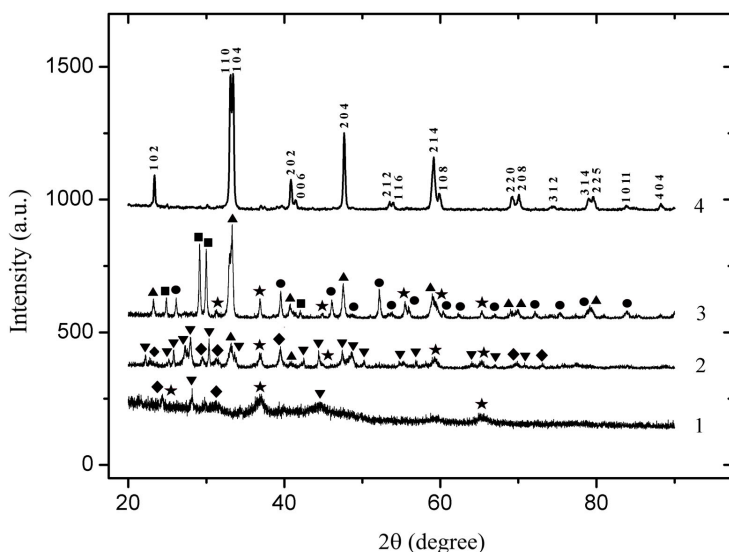


Figure 12. Illustration of the change in the diffractogram of the $\text{La}_{1-3x}\text{M}_{2x}\text{CoO}_{3\pm A}$ ($M = \text{Ca}$; $x = 0.05$) with temperature: 1 – 400°C; 2 – 600°C; 3 – 700°C and 4 – 750°C

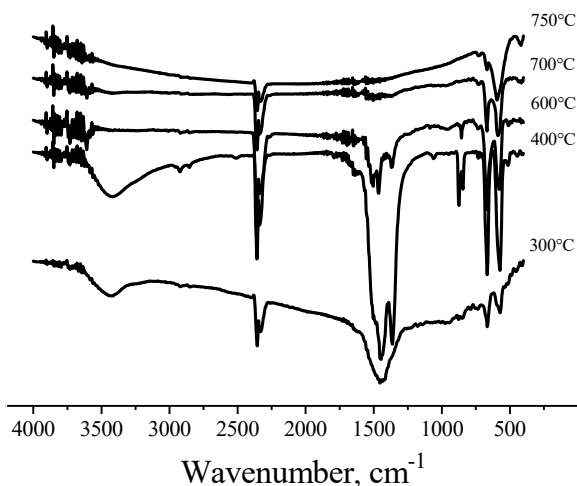


Figure 13. Evolution of the infrared spectrum of the $\text{La}_{1-3x}\text{M}_{2x}\text{CoO}_{3-\Delta}$ ($\text{M} = \text{Ca}$; $x = 0.05$) with temperature

Cation-deficient lanthanum cobaltates formed during thermochemical transformation of the hydroxo-oxalate precursors (750°C, 36 h). Diffraction patterns of calcined precursors showed reflections belonging not to pure metal oxides but to oxide compounds of composition $\text{La}_{0.85}\square_{0.05}\text{M}_{0.1}\text{CoO}_{3-\Delta}$ (\square is a cation vacancy; $\text{M} = \text{Ca}, \text{Sr}, \text{Ba}$). Indexing of the X-ray powder patterns (hexagonal setting) showed that the substituted cobaltates were isostructural with the base LaCoO_3 perovskite matrix. The crystallographic parameters (space group $R\text{-}3c$) increased smoothly in the order of increasing average ionic radius of $\text{Ca}\text{-Sr}\text{-Ba}$ upon partial heterovalent substitution $\text{La}^{3+}/\text{M}^{2+}$ (Table 2).

Table 2

Crystallographic parameters of $\text{La}_{1-3x}\square_x\text{M}_{2x}\text{CoO}_{3-\Delta}$ ($\square = \text{vacancy}$; $\text{M} = \text{Ca}, \text{Sr}, \text{Ba}$) obtained by annealing a hydroxo-oxalate precursor

Alkaline earth metal	$a, \text{\AA}$	$c, \text{\AA}$	$V, \text{\AA}^3$
Ca	5,428(1)	13,091(6)	334,0(3)
Sr	5,437(2)	13,156(9)	336,8(5)
Ba	5,439(1)	13,210(9)	338,5(6)

Thus, the synthesized solid solutions $\text{La}_{1-3x}\text{Li}_x\text{M}_{2x}\text{CoO}_{3-\Delta}$ ($\text{M} = \text{Ca}, \text{Sr}, \text{Ba}; 0 \leq x \leq 0.05$) could be viewed as cation-deficient perovskite-type matrices $\text{La}_{1-3x}\square_x\text{M}_{2x}\text{CoO}_{3-\Delta}$ ($\text{M} = \text{Ca}, \text{Sr}, \text{Ba}; 0 \leq x \leq 0.05$) doped with Li.

3. Structural features of substituted perovskites based on LaMO_3 ($\text{M} = \text{Mn}, \text{Fe}, \text{Co}$)

Figure 14 shows the powder diffraction patterns of lanthanum-sodium manganite $\text{La}_{0.8}\text{Na}_{0.2}\text{MnO}_3$ ($x = 0$) obtained at different sintering temperatures (500°C, 700°C and 900°C). No peaks corresponding to impurity phases were found in the diffraction patterns of the samples. The reflections were indexed in the rhombohedral system (space group $R\bar{3}c$) in accordance with the literature data (JCPDS Card No. 96-152-1820). This confirms that the rhombohedral symmetry of the nanocrystalline samples remains unchanged after the treatment of manganite at the corresponding temperatures.

With increasing temperature of synthesis of samples there is a decrease in parameters of crystal cell (a, c) and volume of unit cell V (Table 3), which may be a consequence of process of thermally induced ordering of ions and/or vacancies of cationic and/or anionic sublattice. X-ray density ρ_{XRD} for manganites nanopowders, calculated from powder diffraction data, and angle Mn-O-Mn increase directly proportional to temperature of isothermal treatment, while distance Mn-O – decreases. This fact may also indicate decrease in defectivity of perovskite structure and simultaneous increase in hybridization 2p-3d between ions O and Mn, exchange interaction between ions Mn-Mn during calcination.

As evidenced by powder X-ray diffraction data, the average sizes of nanoparticles (the sizes of coherent scattering regions) of lanthanum manganites $\text{La}_{0.8-x}\square_x\text{Na}_{0.2}\text{Mn}_{1+x}\text{O}_{3-\Delta}$ ($x = 0$), calculated by the Scherrer method, increase in direct proportion to the synthesis temperature. This dependence indicates that with an increase in the isothermal holding temperature, particle enlargement and agglomeration occur, but even at $T = 900^\circ\text{C}$ the nanocrystallinity of the samples is preserved.

Substituted manganites $\text{La}_{0.8-x}\square_x\text{Na}_{0.2}\text{Mn}_{1+x}\text{O}_{3-\Delta}$, obtained at 500°C, demonstrate the highest dislocation density values, which indicates a low degree of crystallinity of nanoparticles, while after isothermal treatment at

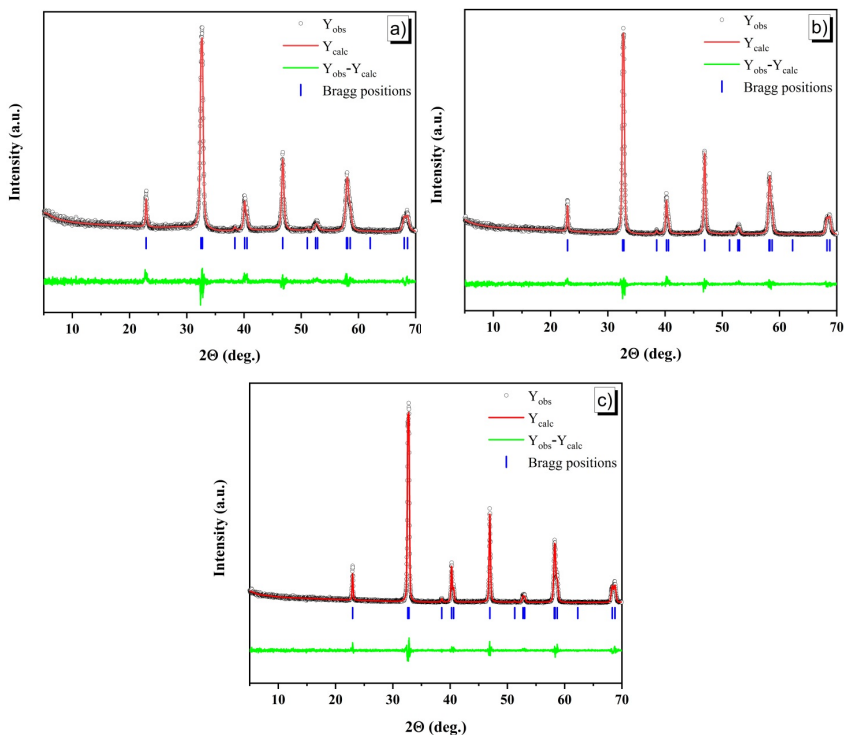


Figure 14. Rietveld refinement XRD patterns of the $\text{La}_{0.8-x}\text{Na}_{0.2}\text{MnO}_3$ samples obtained under different annealing temperatures $t_{\text{ann}} = 500$ (a), 700 (b), and 900 °C (c). The experimental (circles) and calculated (red line) values with a difference (blue line) are plotted.

The vertical bars indicate the angular positions of the allowed Bragg reflections (JCPDS No. 96-152-180)

700°C the manganites show intermediate dislocation density values, which confirms the formation of well-crystallized compounds. However, samples synthesized at 900°C have the lowest dislocation density values, indicating an increase in the crystallinity of the nanoparticles.

The diffraction patterns of $\text{La}_{0.8-x}\text{Na}_x\text{Mn}_{1+x}\text{O}_{3-\Delta}$ nanopowders, refined by the Rietveld method, and their crystal structure are shown in Figure 15a-b. Solid solutions of $\text{La}_{0.8-x}\text{Na}_x\text{Mn}_{1+x}\text{O}_{3-\Delta}$ ($0 \leq x \leq 0.2$)

are indexed in the rhombohedral crystal system (space group $R\bar{3}c$) in accordance with ICSD card No. 01-080-3121.

Table 3
Crystallographic parameters for $\text{La}_{0.8}\text{Na}_{0.2}\text{MnO}_3$ nanopowder, refined by the Rietveld method

Sample	$\text{La}_{0.8}\text{Na}_{0.2}\text{MnO}_3$		
Sintering temperature [°C]	500	700	900
Crystal system	rhombohedral	rhombohedral	rhombohedral
Space group	$R\bar{3}c$ (No, 167)	$R\bar{3}c$ (No, 167)	$R\bar{3}c$ (No, 167)
Lattice parameters	$a = 5,5103(4) \text{ \AA};$ $b = 5,5103(4) \text{ \AA};$ $c = 13,3480(16) \text{ \AA};$ $\alpha = \beta = 90^\circ;$ $\gamma = 120^\circ$	$a = 5,4891(12) \text{ \AA};$ $b = 5,4891(12) \text{ \AA};$ $c = 13,3213(29) \text{ \AA};$ $\alpha = \beta = 90^\circ;$ $\gamma = 120^\circ$	$a = 5,4878(1) \text{ \AA};$ $b = 5,4878(1) \text{ \AA};$ $c = 13,3198(5) \text{ \AA};$ $\alpha = \beta = 90^\circ;$ $\gamma = 120^\circ$
Unit cell volume $V [\text{\AA}^3]$	351,001(62)	347,602(132)	347,398(17)
Number of formula units Z	6	6	6
Bond length $\langle d_{\text{Mn-O}} \rangle [\text{\AA}]$	1,9642(21)	1,9523(20)	1,9524(17)
Bond angle $\theta_{\langle \text{Mn-O-Mn} \rangle} [^\circ]$	162,31(29)	164,62(28)	164,39(24)
X-Ray density $\rho_x [\text{g/cm}^3]$	6,207	6,268	6,271
R_p [%]	10,1	9,23	9,37
R_{wp} [%]	13,7	13,8	14,1
R_{exp} [%]	11,88	11,96	11,87
χ^2 [%]	1,33	1,32	1,40

The diffraction patterns of $\text{La}_{0.8-x}\text{Na}_x\text{Mn}_{1+x}\text{O}_{3-\Delta}$ nanopowders, refined by the Rietveld method, and their crystal structure are shown in Figure 15a-b. Solid solutions of $\text{La}_{0.8-x}\text{Na}_x\text{Mn}_{1+x}\text{O}_{3-\Delta}$ ($0 \leq x \leq 0.2$) are indexed in the rhombohedral crystal system (space group $R\bar{3}c$) in accordance with ICSD card No. 01-080-3121.

According to the results of transmission electron microscopy (TEM) for $\text{La}_{0.8-x}\text{Na}_x\text{Mn}_{1+x}\text{O}_{3-\Delta}$ nanopowders (see Figure 15c-g), the average size of spherical particles d is $d = 73 \text{ nm}$ ($x = 0.00$), 55 nm ($x = 0.05$),

48 nm ($x = 0.10$), 62 nm ($x = 0.15$) and 69 nm ($x = 0.20$), which correlates with the size of the coherent scattering region D_s (at $x \leq 0.10$), calculated based on powder diffraction data according to the Scherrer equation. The discrepancies between TEM and X-ray diffraction data for other samples with increased overstoichiometric manganese content $x > 0.10$ may be due to the presence of an impurity phase Mn_3O_4 and the difficulty in determining the true size due to magnetic attraction between nanoparticles. The high-resolution TEM images clearly show the interplanar lattice spacing of well-crystallized nanoparticles with an average size of 0.381 nm, determined from the intensity profile of the lattice plane corresponding to the (012) plane (see Figure 15h).

The X-ray density ρ_{XRD} for the composition with $x = 0.2$ (5.753 g/cm³), calculated from powder diffraction data, decreases by 7.5% relative to the stoichiometric manganite $La_{0.8}Na_{0.2}MnO_{3-\Delta}$ (6.221 g/cm³). This fact may indicate an increase in the defectiveness of the perovskite structure of non-stoichiometric manganites.

The concentration dependence of the lattice parameters for $La_{0.8-x}\square_xNa_{0.2}Mn_{1+x}O_{3-\Delta}$ ($0 \leq x \leq 0.2$) is given in Table 4. With an increase in the overstoichiometric manganese content and the concentration of cation vacancies in the A-position, an additional ferrimagnetic phase Mn_3O_4 with the tetragonal space group $I41/amd$ is formed (ICSD card No. 01-071-6262). This demonstrates the existence of a solubility limit for overstoichiometric manganese up to $x < 0.10$ in the $La_{0.8-x}\square_xNa_{0.2}Mn_{1+x}O_{3-\Delta}$ nanopowder.

On the one hand, the creation of only cation vacancies ≥ 0.09 already leads to the appearance of the second phase Mn_3O_4 and, on the other hand, at a concentration of superstoichiometric manganese ≤ 0.10 , the manganite system remains single-phase.

According to the established defect formation mechanism for the real structure of perovskite with vacancy-type point defects (cationic $V^{(c)}$ and anionic $V^{(a)}$ vacancies) [14], overstoichiometric manganese can occupy cation-deficient A- and B-positions in the form of Mn_A^{2+} and Mn_B^{3+} / Mn_B^{4+} ions, respectively. The appearance of Mn^{2+} ions was observed earlier for similar A-cation-deficient manganites [12; 13]. Mn^{2+} ions with an effective ionic radius of 1.13 Å for coordination number (CN) = 12 occupy the A-position together with larger La^{3+} (1.36 Å) and Na^+ (1.39 Å) ions

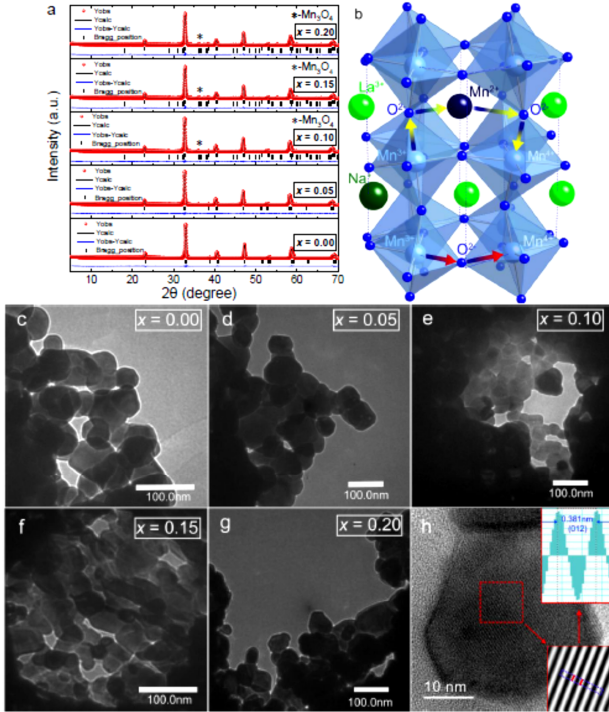


Figure 15. Evolution of XRD patterns and morphology in the $\text{La}_{0.8-x}\text{Na}_x\text{Mn}_{1+x}\text{O}_{3-A}$ nanoparticles with a perovskite structure:

(a) XRD patterns measured at room temperature and fitted by Rietveld method show the preserving rhombohedral $R\bar{3}c$ structure (upper bars) and the nucleation of hausmannite Mn_3O_4 second-phase (down bars) as both the overstoichiometric manganese content and the concentration of cation vacancies on A-position $V_A^{(c)}$ increase;

(b) The general scheme of unit cell shows the location of (La^{3+} , Na^+ , Mn^{2+}) cations on A-, (Mn^{3+} , Mn^{4+}) cations on B- and anions (O^{2-}) on X-sites of the perovskite structure with possible mechanisms of double exchange $\text{Mn}^{3+} \leftrightarrow \text{O}^{2-} \leftrightarrow \text{Mn}^{4+}$ and multiple double exchange $\text{Mn}^{3+} \leftrightarrow \text{O}^{2-} \leftrightarrow \text{Mn}^{2+} \leftrightarrow \text{O}^{2-} \leftrightarrow \text{Mn}^{4+}$;

(c-g) TEM images show a non-monotonic change in the size of spherical-like nanoparticles with increase in x ;

(h) HRTEM image indicates well-developed crystalline structure of nanoparticles with 0.381 nm corresponding to (012) plane determined from lattice plane intensity profile using the fast Fourier transformation

(see Figure 15b), which leads to distortion of the perovskite structure [16]. The presence of Mn^{2+} ions in real defective manganites may additionally be associated with the charge disproportionation model, i.e., the appearance of more stable $Mn^{2+} + Mn^{4+}$ pairs instead of $Mn^{3+} + Mn^{3+}$.

Table 4

Structural parameters of $La_{0.8-x}Na_xMn_{1+x}O_{3-\Delta}$ nanopowders, refined by the Rietveld method at room temperature

x	0.00	0.05	0.10	0.15	0.20
Oxygen index					
«O _{3-Δ} »	2.96	2.96	2.95	2.95	2.93
Coherent scattering region					
D (HM)	61	60	56	55	53
Phase composition	single-phase	single-phase	~2 % Mn ₃ O ₄	~5 % Mn ₃ O ₄	~6 % Mn ₃ O ₄
Cell parameters					
a (Å)	5.4784(1)	5.4772(1)	5.4775(1)	5.4789(1)	5.4775(1)
c (Å)	13.3166(2)	13.3183(2)	13.3179(3)	13.3214(3)	13.3178(3)
V (Å ³)	346.125(8)	346.020(8)	346.046(9)	346.316(11)	346.043(11)
Positional parameters					
O(18e) x	0.4574(12)	0.4571(12)	0.4547(11)	0.4550(13)	0.4544(14)
Bond distance <d_{Mn-O}> (Å)					
Mn _B ^{3+/4+} – O ²⁻	1.9458(50)	1.9454(50)	1.9474(46)	1.9478(55)	1.9475(59)
La _A ³⁺ / Na _A ⁺ / Mn _A ²⁺ – O ²⁻	2.5057(66)	2.5038(66)	2.4905(60)	2.4928(71)	2.4889(77)
Bond angle Mn–O–Mn (°)					
Mn _B ^{3+/4+} – O ²⁻ – Mn _B ^{3+/4+}	166.22(22)	166.13(22)	165.36(20)	165.46(24)	165.27(26)
La _A ³⁺ / Na _A ⁺ / Mn _A ²⁺ – O ²⁻ – Mn _B ^{3+/4+}	96.89(15)	96.94(15)	97.32(14)	97.27(16)	97.37(18)
Agreement factors					
R _{wp} (%)	11.8	13.2	13.8	15.8	16.2
R _p (%)	7.27	9.49	10.00	11.3	11.2
R _{exp} (%)	6.67	9.39	9.59	9.52	9.51
χ ² = (R _{wp} /R _{exp}) ²	2.42	1.97	2.08	2.76	2.90

As shown in Table 4, the unit cell volume tends to decrease with increasing x. A similar behavior was observed for A-deficient manganites [13]. One of the interesting features obtained from the structural data is the

change in the bond distance and angle depending on x , which plays a decisive role in the magnetotransport properties of manganites. To establish the regularities between the structural and magnetic properties of $\text{La}_{0.8-x}\text{Na}_{0.2}\text{Mn}_{1+x}\text{O}_{3-\Delta}$, the bond distances $\langle d_{\text{Mn-O}} \rangle$ for $\text{Mn}_B^{3+/4+} - \text{O}^{2-} / \text{La}_A^{3+} / \text{Na}_A^+ / \text{Mn}_A^{2+} - \text{O}^{2-}$ and the Mn-O-Mn angles for $\text{Mn}_B^{3+/4+} - \text{O}^{2-} - \text{Mn}_B^{3+/4+} / \text{La}_A^{3+} / \text{Na}_A^+ / \text{Mn}_A^{2+} - \text{O}^{2-} - \text{Mn}_B^{3+/4+}$ between the corresponding positions of Mn ions at the A- and B-positions and oxygen were determined taking into account the data of iodometric titration with a certain concentration $V^{(a)}$ and excluding the influence of Mn_3O_4 of the second phase. With increasing x , the lattice parameters and $\langle d_{\text{Mn-O}} \rangle$ ($\text{La}_A^{3+} / \text{Na}_A^+ / \text{Mn}_A^{2+} - \text{O}^{2-}$) decrease, which indicates the appearance of [16]. The tendency to increase $\langle d_{\text{Mn-O}} \rangle$ ($\text{Mn}_B^{3+/4+} - \text{O}^{2-}$) and decrease the angle Mn-O-Mn ($\text{Mn}_B^{3+/4+} - \text{O}^{2-} - \text{Mn}_B^{3+/4+}$) should lead to a narrowing of the band width $W \sim \cos\theta \cdot \langle d_{\text{Mn-O}} \rangle^{-3,5}$, weak double exchange and, accordingly, a decrease in T_C . However, on the other hand, $\langle d_{\text{Mn-O}} \rangle$ for $\text{Mn}_B^{3+/4+} - \text{O}^{2-}$ (at small $x < 0.10$) and $\text{La}_A^{3+} / \text{Na}_A^+ / \text{Mn}_A^{2+} - \text{O}^{2-}$ decreases and the angle Mn-O-Mn for $\text{La}_A^{3+} / \text{Na}_A^+ / \text{Mn}_A^{2+} - \text{O}^{2-} - \text{Mn}_B^{3+/4+}$ increases, which favorably affects the magnetotransport properties of manganites due to Mn_A^{2+} ions participating in multiple double exchange [13; 16]. Thus, different mechanisms of exchange interaction and their strength determine the magnetic behavior of $\text{La}_{0.8-x}\text{Na}_{0.2}\text{Mn}_{1+x}\text{O}_{3-\Delta}$ ($0 \leq x \leq 0.2$).

In order to determine the effect of simultaneous substitution of lanthanum by singly charged Na^+ and doubly charged Cd^{2+} on the crystal structure of lanthanum manganites, the change in crystal lattice parameters was investigated, the phase composition and structural features of magnetic nanopowders $\text{La}_{0.8-x}\text{Cd}_x\text{Na}_{0.2}\text{MnO}_3$ ($0 \leq x \leq 0.05$).

It was found that all manganites are single-phase and retain the perovskite structure with rhombohedral symmetry (space group $R\bar{3}c$). A careful analysis of the diffraction patterns of $\text{La}_{0.8-x}\text{Cd}_x\text{Na}_{0.2}\text{MnO}_3$ ($x = 0; 0.05$) powders obtained at different temperatures (500, 700 and 900°C) showed that characteristic peak splittings did not appear in the diffraction patterns, which indicates a rhombohedral disordered structure for the entire range of substitutions studied. The diffraction peaks of the cadmium-substituted samples exactly match those of the pure unsubstituted $\text{La}_{0.8}\text{Na}_{0.2}\text{MnO}_3$ sample. This confirms that the rhombohedral symmetry

of the nanocrystalline samples remains unchanged after partial La/Cd substitution and annealing of manganite at the appropriate temperatures.

Refinement of instrumental, crystallographic parameters, pseudo-Voigt profile function parameters for the samples was carried out by the Rietveld method. Analysis of the obtained results showed that with increasing synthesis temperature of $\text{La}_{0.8}\text{Na}_{0.2}\text{MnO}_3$ and $\text{La}_{0.75}\text{Cd}_{0.05}\text{Na}_{0.2}\text{MnO}_3$ samples, there is a decrease in the crystal cell parameters (a , c) and the unit cell volume V , which may be a consequence of the process of thermally induced ordering of ions and/or vacancies of the cationic and/or anionic sublattice. The X-ray density for manganite nanopowders, calculated from powder diffraction data, and the Mn-O-Mn angle increase in direct proportion to the isothermal treatment temperature, while the Mn-O distance decreases. This fact may also indicate a decrease in the defectivity of the perovskite structure and a simultaneous increase in 2p-3d hybridization between O and Mn ions, exchange interaction between Mn-Mn ions both during partial non-isovalent substitution of lanthanum by cadmium and during heat treatment.

Figure 16(a)–16(c) shows the Rietveld refined XRD patterns of the sintered samples of the $\text{La}_{1-x}\text{Sr}_x\text{MnO}_3$ ($0.23 \leq x \leq 0.33$) nanopowders. No secondary phases could be detected, within the sensitivity limits of the experiment. The refined XRD patterns show that the samples are in single phase form. The Rietveld refinements were carried out on the basis of a rhombohedral unit cell (space group $R\bar{3}c$) then get an acceptable R value. The background was fitted with shifted Chebyshev polynomial function, and pseudo-Voigt function was employed to model the peak shapes in all cases. In the refinement, the oxygen positions (x), lattice constants, isothermal parameters, scale factors, and shape parameters have been taken as free parameters. However, all other atomic positions have been taken as fixed. The refined lattice parameters and unit cell volumes for samples LSM023, LSM028 and LSM033 have been listed in Table 5 along with the errors in parentheses. It was observed that lattice parameters and unit cell volume decrease with increasing substitution degree (Sr content), which are comparable to the values reported in the literature [28].

**Rietveld refinement crystallographic parameters
for $\text{La}_{1-x}\text{Sr}_x\text{MnO}_3$ ($0.23 \leq x \leq 0.33$) nanopowders**

Sample	$\text{La}_{0.77}\text{Sr}_{0.23}\text{MnO}_3$	$\text{La}_{0.72}\text{Sr}_{0.28}\text{MnO}_3$	$\text{La}_{0.67}\text{Sr}_{0.33}\text{MnO}_3$
Crystal system	rhombohedral	rhombohedral	rhombohedral
Space group	$R\bar{3}c$ (No. 167)	$R\bar{3}c$ (No. 167)	$R\bar{3}c$ (No. 167)
Lattice parameters	$a = 5.50195(22) \text{ \AA}$; $b = 5.50195(22) \text{ \AA}$; $c = 13.34439(94) \text{ \AA}$; $\alpha = \beta = 90^\circ$; $\gamma = 120^\circ$	$a = 5.50006(21) \text{ \AA}$; $b = 5.50006(21) \text{ \AA}$; $c = 13.34106(83) \text{ \AA}$; $\alpha = \beta = 90^\circ$; $\gamma = 120^\circ$	$a = 5.49235(35) \text{ \AA}$; $b = 5.49235(35) \text{ \AA}$; $c = 13.34518(150) \text{ \AA}$; $\alpha = \beta = 90^\circ$; $\gamma = 120^\circ$
Unit cell volume $V [\text{\AA}^3]$	349.835(32)	349.507(29)	348.635(50)
Z	6	6	6
Bond distance $\langle d_{\text{Mn-O}} \rangle [\text{\AA}]$	1.9520(25)	1.9495(26)	1.9461(26)
Bond angle $\theta_{\langle \text{Mn-O-Mn} \rangle} [^\circ]$	166.7(5)	167.7(3)	168.7(3)
Bandwidth W	0.0956	0.0961	0.0968
X-Ray density $\rho_x [\text{g}\cdot\text{cm}^{-3}]$	6.552	6.485	6.428
R_p [%]	6.53	6.80	7.61
R_{wp} [%]	8.44	8.76	9.81
R_{exp} [%]	7.39	7.82	7.54
χ^2 [%]	1.30	1.26	1.69

At first sight, this would appear very strange since the ionic radius of La^{3+} in 12-fold coordination is 1.36 Å which is smaller than the ionic radius of Sr^{2+} (1.44 Å) [29]. The explanation may probably lie in the nature of the compensating defect for the negatively charged dopant defect [30; 31]. Therefore, the most probable compensating defect is the oxidation of the 6-fold coordinated Mn^{3+} (0.645 Å) to Mn^{4+} (0.53 Å). The accompanied almost 18% reduction is able to accommodate any other expansion effects and leads to a unit cell contraction, as obtained by the XRD results. Conclusively, the XRD results provide a strong indication that the negative charge created by the heterovalent substitutions is compensated by the oxidation of trivalent Mn to tetravalent and not by the creation of oxygen vacancies [30]. The average crystallite sizes of the lanthanum-strontium

manganite, as determined by using Scherrer equation from the peaks with Miller indices (102) in the XRD pattern, are given in Table 6.

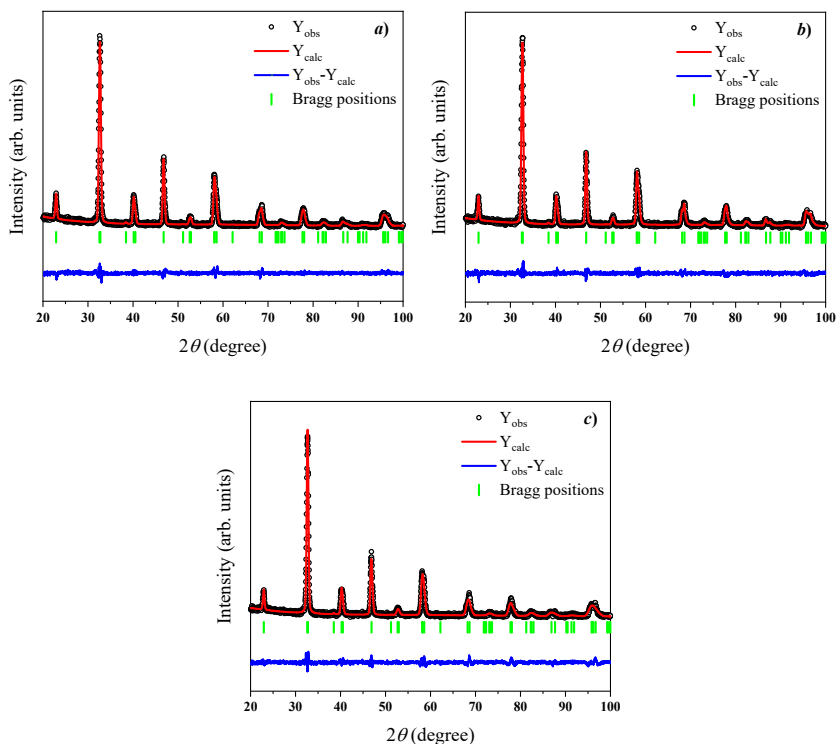


Figure 16. Rietveld refined XRD patterns for samples $La_{0.77}Sr_{0.23}MnO_3$ (a), $La_{0.72}Sr_{0.28}MnO_3$ (b) and $La_{0.67}Sr_{0.33}MnO_3$ (c) synthesized by sol-gel method. The observed experimental diffractograms are given by the red lines (Y_{obs}), the black lines (Y_{calc}) are calculated diffractograms, and the residual lines ($Y_{obs} - Y_{calc}$) are shown in blue color. The vertical green bars indicate the angular positions of the allowed Bragg reflections

The bandwidth is characterized by the overlap between the Mn-3d orbital and O-2p orbital in the MnO₆ oxygen octahedra and can be described empirically by an equation [32]:

$$W = \frac{\cos\beta}{(d_{Mn-O})^{3.5}}, \quad (12)$$

where $\beta = (\pi - \theta_{<Mn-O-Mn>})/2$, d_{Mn-O} is the average Mn-O bond length, and $\theta_{<Mn-O-Mn>}$ is the average Mn-O-Mn bond angle.

Table 6

**Experimental parameters of the Scherrer formula
for determining average size of the coherent scattering regions D_s
and dislocation density δ in the lanthanum-strontium manganites**

Sample	2 θ , degree	β , radian	cos θ	λ , nm	K	$\langle D_s \rangle$, nm	$\delta \cdot 10^4$, nm ⁻²
LSM023	22.917	0.0017	0.980	0.15406	0.9	81±2	1.5
LSM028	22.924	0.0014	0.980	0.15406	0.9	103±6	0.9
LSM033	22.943	0.0012	0.980	0.15406	0.9	114±5	0.8

Figure 17 depict the observed, calculated and difference room temperature PXRD profiles of the La_{0.7}Ag_{0.2}Mn_{1.1}O₃ nanoparticles synthesized using different temperatures: 900°C (LAM900) and 1000°C (LAM1000). It can be seen that the profiles for observed and calculated one are perfectly matching. The value of χ^2 comes out to be equal to 2, which may be considered to be very good for estimations. The profile fitting procedure adopted was minimizing the χ^2 function.

From the powder diffraction data and the refined Rietveld analysis it is cleared that the LAM900 sample contains two impurity phases, namely hexagonal lanthanum hydroxide La(OH)₃ (JCPDS no. 96-403-1382) and cubic silver Ag (JCPDS no. 96-110-0137). This agrees very well with our previous results [33]. It has been established that the relative proportions of the rhombohedral perovskite phase and the cubic phase of silver in the samples depend on the temperature of the sintering process. So, as the isothermal holding temperature increases from 900°C to 1000°C, the silver content decreases by approximately 30%, and the peaks from lanthanum hydroxide completely disappear from the diffraction pattern of LAM1000. Since the melting temperature of silver is 962°C, it can be assumed that at

a synthesis temperature of 1000°C, silver crystallizes in the form of a thin film at the bottom of the crucible, as can be seen from the Figure 18.

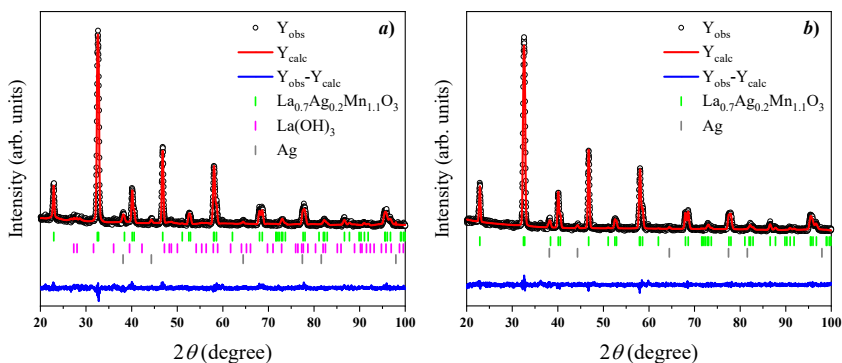


Figure 17. Rietveld refined XRD patterns for sample $\text{La}_{0.7}\text{Ag}_{0.2}\text{Mn}_{1.1}\text{O}_3$ synthesized by nitrate pyrolysis method at 900°C (a) and 1000°C (b). The observed experimental diffractograms are given by the red lines (Y_{obs}), the black lines (Y_{calc}) are calculated diffractograms, and the residual lines ($Y_{\text{obs}} - Y_{\text{calc}}$) are shown in blue color. The vertical green bars indicate the angular positions of the allowed Bragg reflections

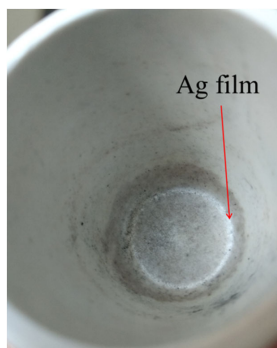


Figure 18. Formation of a silver film at the bottom of the crucible after annealing of lanthanum-silver manganite at 1000°C for 5 hours

Table 7
Rietveld refinement crystallographic parameters for $\text{La}_{0.7}\text{Ag}_{0.2}\text{Mn}_{1.1}\text{O}_3$ nanopowders synthesized at different temperatures

Sample	LAM900			LAM1000	
	Sintering temperature [°C]	900	1000		
Phase composition	$\text{La}_{0.7}\text{Ag}_{0.2}\text{Mn}_{1.1}\text{O}_3$ (97.3%)	$\text{La}(\text{OH})_3$ (0.4%)	Ag (2.3%)	$\text{La}_{0.7}\text{Ag}_{0.2}\text{Mn}_{1.1}\text{O}_3$ (98.4%)	Ag (1.6%)
Crystal system	rhombohedral	hexagonal	cubic	rhombohedral	
Space group	$R\bar{3}c$ (No. 167)	$P6_3/m$ (No. 176)	$Fm\bar{3}m$ (No. 225)	$R\bar{3}c$ (No. 167)	$Fm\bar{3}m$ (No. 225)
Lattice parameters	$a = 5.5063(1) \text{ \AA};$ $b = 5.5063(1) \text{ \AA};$ $c = 13.3347(6) \text{ \AA};$ $\alpha = \beta = 90^\circ;$ $\gamma = 120^\circ$	$a = 6.5257(57) \text{ \AA};$ $b = 6.5257(57) \text{ \AA};$ $c = 3.8498(44) \text{ \AA};$ $\alpha = \beta = 90^\circ;$ $\gamma = 120^\circ$	$a = 4.0848(1) \text{ \AA};$ $b = 4.0848(1) \text{ \AA};$ $c = 4.0848(1) \text{ \AA};$ $\alpha = \beta = \gamma = 90^\circ$	$a = 5.5101(1) \text{ \AA};$ $b = 5.5101(1) \text{ \AA};$ $c = 13.3387(5) \text{ \AA};$ $\alpha = \beta = 90^\circ;$ $\gamma = 120^\circ$	$a = 4.0844(8) \text{ \AA};$ $b = 4.0844(8) \text{ \AA};$ $c = 4.0844(8) \text{ \AA};$ $\alpha = \beta = \gamma = 90^\circ$
Unit cell volume $V [\text{\AA}^3]$	350.14(2)	141.98(24)	68.15(4)	350.72(2)	68.14(2)
Z	6	2	4	6	4
X-Ray density ρ_x [g·cm ⁻³]	6.466	4.443	10.513	6.455	10.515
R_p [%]		6.77			6.25
R_{wp} [%]		8.81			8.33
R_{exp} [%]		7.54			7.47
χ^2 [%]		1.37			1.24

The lattice parameters as obtained for LAM900 and LAM1000 nanopowders are in good agreement with the literature report [33-35]. It was observed that lattice parameters (a , c) increase with increasing calcination temperature. When the sintering temperature increased from 900°C to 1000°C, a minor increase in unit cell volume (V) was noticed.

However, if the synthesis of silver-containing manganites is carried out in a conventional chemical glass beaker, then according to the data of powder X-ray diffraction, it was possible to obtain samples that do not contain silver impurities. As can be seen from Figure 19a, after heat treatment at 750°C, a single-phase substituted manganite is formed. There are no peaks of impurity phases in the diffractogram. Although, when calcined at 800°C, in addition to the reflexes of the perovskite phase, manganese oxide patterns are observed (Figure 19b). The reflexes of metallic silver are not detected in any of the diffractograms.

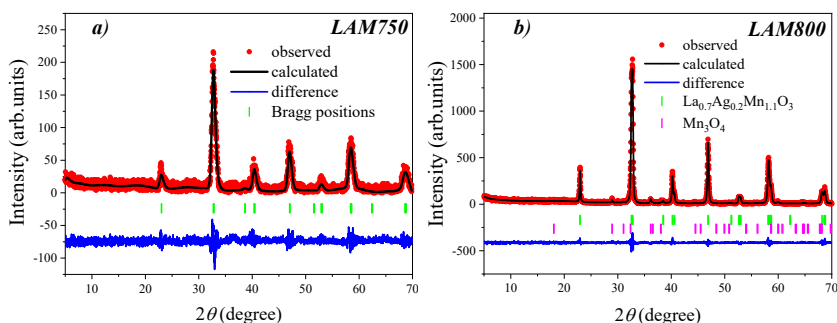


Figure 19. XRD patterns of the LAM750 and LAM800 manganite nanopowders at room temperature refined by the Rietveld method

With the simultaneous substitution of triple-charged lanthanum for double-charged strontium and the introduction of superstoichiometric manganese in the B-position, it was possible to obtain single-phase manganite $\text{La}_{0.6}\text{Sr}_{0.3}\text{Mn}_{1.1}\text{O}_3$, the crystal structure of which was established for the first time. According to the X-ray diffraction data (Figure 20), the $\text{La}_{0.6}\text{Sr}_{0.3}\text{Mn}_{1.1}\text{O}_3$ nanopowder has a rhombohedrally deformed perovskite structure (space group $R\bar{3}c$) with the structural parameters given in tables 8-9.

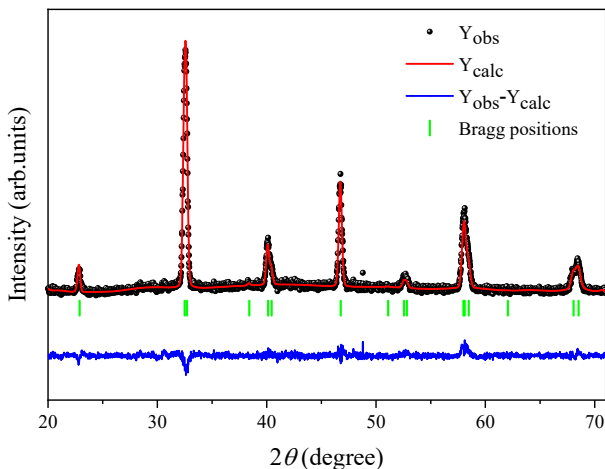


Figure 20. Rietveld refined diffractogram of $\text{La}_{0.6}\text{Sr}_{0.3}\text{Mn}_{1.1}\text{O}_3$.

Based on the mechanism of defect formation and the data in table 9, the molar formula of the nanopowder has the following form $\left\{ \text{La}_{0.58}^{3+} \text{Sr}_{0.29}^{2+} \text{Mn}_{0.05}^{2+} \text{V}^{(c)}_{0.08} \right\}_A \left[\text{Mn}_{0.66}^{3+} \text{Mn}_{0.34}^{4+} \right]_B \text{O}_{2.88}^{2-} \text{V}^{(a)}_{0.12}$ and real density $\rho_p = 5.957 \text{ g/cm}^3$.

It is established that the real structure contains ions of different valences Mn_B^{4+} , Mn_B^{3+} , Mn_A^{2+} , as well as cationic $\text{V}^{(c)}$ and anionic $\text{V}^{(a)}$ vacancies. In addition, the data of X-ray structural studies (Table 9) show that part of the non-stoichiometric manganese passes from the B-position to the A-position, i.e. the appearance of non-stoichiometric manganese in the composition of the substituted manganite leads to even greater charge disorder in the perovskite structure.

4. Role of dopants and synthesis condition on properties of perovskites

For solid solutions in the system $\text{La}_{1-x}\text{Me}_x\text{CoO}_3$ (Me=Ca, Sr, Ba) it is known that they exist in the whole range of substitutions. The magnitude of the rhombohedral distortion decreases with increasing alkaline earth metal content and at $x = 0.5$ the compositions take a cubic structure.

Table 8

Crystallographic parameters of $\text{La}_{0.6}\text{Sr}_{0.3}\text{Mn}_{1.1}\text{O}_3$ nanopowder, refined by the Rietveld method

Sample	$\text{La}_{0.6}\text{Sr}_{0.3}\text{Mn}_{1.1}\text{O}_3$
Crystal system	rhombohedral
Space group	$R\bar{3}c$ (No. 167)
Lattice parameters	$a = 5.50527(24) \text{ \AA};$ $b = 5.50527(24) \text{ \AA};$ $c = 13.36876(89) \text{ \AA}$
Unit cell volume $V [\text{\AA}^3]$	350.896(32)
Number of formula units Z	6
X-Ray density $\rho_{\text{XRD}} [\text{g/cm}^3]$	6.192
R_p [%]	6.40
R_{wp} [%]	7.95
R_{exp} [%]	6.70
R_{Bragg} [%]	6.51
R_f [%]	5.99
χ^2 [%]	1.41

Table 9

Refined atomic coordinates in the structure of substituted $\text{La}_{0.6}\text{Sr}_{0.3}\text{Mn}_{1.1}\text{O}_3$ lanthanum manganite

Atomic position	Atom symbol	x	y	z	Occupancy
Mn1	Mn	0	0	0	1.00
La1	La	0	0	0.25	0.59
Sr1	Sr	0	0	0.25	0.29
Mn2	Mn	0	0	0.25	0.10
O1	O	0.538(3)	0	0.25	0.99

The X-ray powder diffraction patterns of $\text{La}_{1-3x}\text{Li}_x\text{M}_{2x}\text{CoO}_{3-\delta}$ ($M = \text{Ca}, \text{Sr}, \text{Ba}; 0 \leq x \leq 0.1$) samples are shown in Figure 21. It can be seen that the cobaltates of lanthanum, modified by alkali earth metals and lithium, have at room temperature rhombohedrally distorted perovskite cell (SG $R\bar{3}c$) with the parameters shown in Table 10. When lithium and alkali earth metal ions are introduced into the structure of the initial $\text{LaCoO}_{3-\Delta}$, there is a slight increase in the parameters of the unit cell associated with the

change in the ionic radius of the substituent. It should be noted that due to the slight difference in the ionic radii of the La^{3+} and Ca^{2+} cations, the lattice parameters do not really change during the transition from the initial matrix to Ca-containing cobaltates.

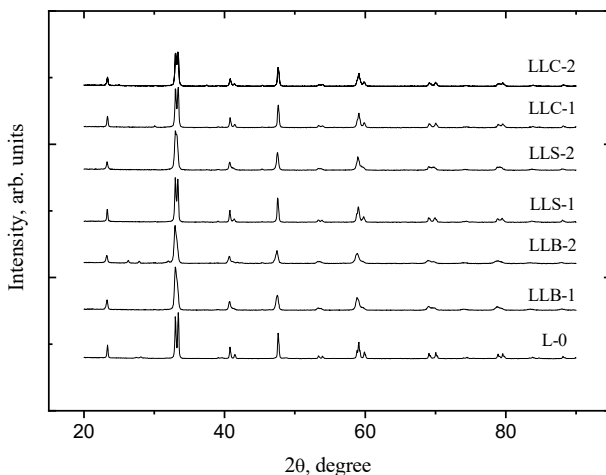


Figure 21. The X-ray powder diffraction patterns of $\text{La}_{1-3x}\text{Li}_x\text{M}_{2x}\text{CoO}_{3-\delta}$: L-0 ($x = 0$), LLB-1 ($\text{M} = \text{Ba}$; $x = 0.05$), LLB-2 ($\text{M} = \text{Ba}$; $x = 0.1$), LLS-1 ($\text{M} = \text{Sr}$; $x = 0.05$), LLS-2 ($\text{M} = \text{Sr}$; $x = 0.1$), LLC-1 ($\text{M} = \text{Ca}$; $x = 0.05$) and LLC-2 ($\text{M} = \text{Ca}$; $x = 0.1$)

The crystallites size D_s of (102) planes of complex oxides were calculated from X-ray diffraction data on the expansion of the diffraction maximum with an angle of $2\theta \approx 23.3$. As can be seen from Table 10, the average value of D_s varied from 32 nm to 73 nm depending on the steric factor of the modifying additives. Thus, the obtained data confirm the fact of formation of nanoparticles of substituted cobaltates of lanthanum.

Figure 22 shows SEM images of the surface of nanocrystalline solid solutions $\text{La}_{1-3x}\text{Li}_x\text{M}_{2x}\text{CoO}_{3-\Delta}$ ($\text{M} = \text{Ca}, \text{Sr}, \text{Ba}$; $0 \leq x \leq 0.05$). These data suggested that the grains of substituted cobaltates were plate-like hexagonal prisms. The average size of the individual particles was $\sim 10^2$ nm. A comparison of the SEM results (D_{SEM}) and the grain sizes obtained from

the diffraction experiment (D_s) indicated that the compounds were mainly particle aggregates (Table 10).

Table 10

Unit cell parameters and grain sizes of oxides with perovskite structure $\text{La}_{1-3x}\text{Li}_x\text{M}_{2x}\text{CoO}_{3-\delta}$ ($\text{M} = \text{Ca, Sr, Ba}$; $0 \leq x \leq 0.1$)

Sample	Unit cell parameters			D_s , nm	D_{SEM} , nm
	a , nm	c , nm	V , nm ³		
$\text{LaCoO}_{3-\Delta}$ (LC)	0.5438(7)	1.3085(9)	0.3351(1)	73	910
$\text{La}_{0.85}\text{Li}_{0.05}\text{Ca}_{0.1}\text{CoO}_{3-\Delta}$ (LLC1C)	0.5438(2)	1.3084(7)	0.3351(3)	56	810
$\text{La}_{0.7}\text{Li}_{0.1}\text{Ca}_{0.2}\text{CoO}_{3-\Delta}$ (LLC2C)	0.5436(1)	1.3083(4)	0.3353(6)	52	750
$\text{La}_{0.85}\text{Li}_{0.05}\text{Sr}_{0.1}\text{CoO}_{3-\Delta}$ (LLS1C)	0.5441(3)	1.3100(3)	0.3358(2)	48	570
$\text{La}_{0.7}\text{Li}_{0.1}\text{Sr}_{0.2}\text{CoO}_{3-\Delta}$ (LLS2C)	0.5434(2)	1.3162(6)	0.3366(3)	36	430
$\text{La}_{0.85}\text{Li}_{0.05}\text{Ba}_{0.1}\text{CoO}_{3-\Delta}$ (LLB1C)	0.5437(4)	1.3130(4)	0.3362(5)	37	440
$\text{La}_{0.7}\text{Li}_{0.1}\text{Ba}_{0.2}\text{CoO}_{3-\Delta}$ (LLB2C)	0.5443(1)	1.3136(4)	0.3370(6)	32	380

The FTIR spectrum of $\text{LaCoO}_{3-\Delta}$ (Figure 23) exhibited bands for stretching vibrations ($\nu_1 = 605 \text{ cm}^{-1}$, $\nu_2 = 565 \text{ cm}^{-1}$, $\nu_3 = 430 \text{ cm}^{-1}$) of M–O–M bonds. According to the literature [24], two types of structurally nonequivalent (Co^I , Co^{II}) Co^{3+} ions situated in an octahedral oxygen environment occur in a trigonally distorted LaCoO_3 perovskite structure. The $\text{Co}^I - \text{O}$ distance is shorter than that of $\text{Co}^{II} - \text{O}$, i.e., the $\text{Co}^I - \text{O}$ bond is shorter than that of $\text{Co}^{II} - \text{O}$. Considering this, stretching vibrations at the higher frequency ν_1 could be assigned to $\text{Co}^I - \text{O}$ bonds; at the lower frequency ν_2 , to vibrations of $\text{Co}^{II} - \text{O}$ bonds. Apparently, the band at $\nu_3 = 430 \text{ cm}^{-1}$ was due to La–O vibrations with La^{3+} dodecahedral coordination.

The frequencies ν_1 and ν_2 in FTIR spectra of solid solutions $\text{La}_{1-3x}\text{Li}_x\text{M}_{2x}\text{CoO}_{3-\Delta}$ ($\text{M} = \text{Ca, Sr, Ba}$; $0 \leq x \leq 0.05$) at first shifted noticeably in opposite directions and then coalesced ($\nu_s \approx 600 \text{ cm}^{-1}$) as the AEM and Li contents in the base matrix increased. Furthermore, a shoulder at 670 cm^{-1} was observed in spectra of the substituted lanthanum cobaltates. Its appearance was associated with formation of Co^{4+} . The shift of this band to higher frequency was related to an increase of the Co–O bond force constant as a result of the increased effective charge on the cobalt ion.

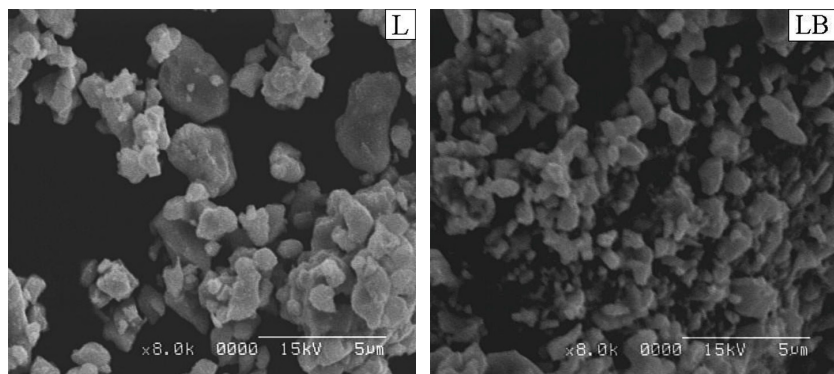


Figure 22. SEM images of the surface of base ($\text{LaCoO}_{3-\Delta}$) (a) and modified ($\text{LaCoO}_3; \text{Li}^+; \text{Ba}^{2+}$) (b) lanthanum cobaltates

The obtained values of the optical band gap for the samples (Figure 24) $\text{La}_{1-3x}\text{Li}_x\text{M}_{2x}\text{CoO}_{3-\delta}$ ($M = \text{Ca}, \text{Sr}, \text{Ba}; x=0.05$) and pure $\text{LaCoO}_{3-\delta}$ are 2.14; 2.07; 2.01 and 2.43 eV, respectively. As the ionic radius of the substituent increases, the width of the optical gap of the band gap narrows. It is known that the introduction of LaCoO_3 alkali earth metals and lithium leads to an increase in oxygen vacancies. As a result, there is an increase in the concentration of carriers, and, accordingly, the approach of the Fermi level to the conduction band of the semiconductor with the subsequent expansion of the band gap. The band on the spectra with $E = 2.07\text{eV}$ corresponds to the $d-d$ -transition of the Co^{2+} ion in the tetrahedral oxygen environment characteristic of spinel Co_3O_4 . Low E_g values indicate the possibility of using lanthanum cobaltates as potential photocatalysts along with classical TiO_2 ($E_g = 3.2\text{eV}$).

Chemical analysis confirmed the existence of the Co^{4+} ion in the compounds, which correlates well with the FTIR spectroscopy data, and the average oxidation state of Co ions (Co^{n+}) varies from $n = 3$ (pure LaCoO_3) to $n > 3$ ($\text{LaCoO}_3; \text{Li}^+; \text{M}^{2+}$). With increasing degree of substitution x , the value of non-stoichiometric oxygen Δ decreases by approximately 0.09 for all compositions.

According to the Goodenough model 3d-holes (Co^{4+}), which are formed by the introduction of a small amount of alkaline earth metal and Li^+ , remain

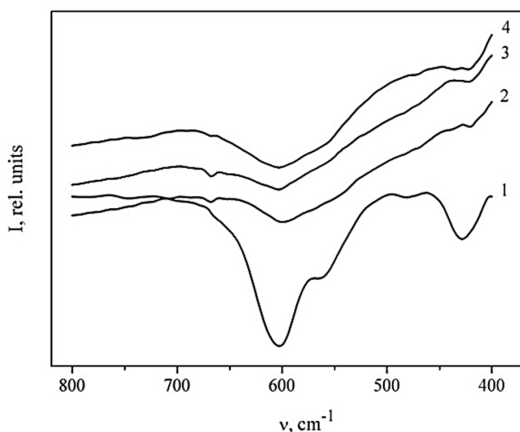


Figure 23. FTIR spectra of solid solutions of the system $\text{La}_{1-3x}\text{Li}_x\text{M}_{2x}\text{CoO}_{3-\delta}$: 1 – $\text{LaCoO}_{3-\delta}$; 2 – $\text{La}_{0.85}\text{Li}_{0.05}\text{Ba}_{0.1}\text{CoO}_{3-\delta}$; 3 – $\text{La}_{0.85}\text{Li}_{0.05}\text{Sr}_{0.1}\text{CoO}_{3-\delta}$; 4 – $\text{La}_{0.85}\text{Li}_{0.05}\text{Ca}_{0.1}\text{CoO}_{3-\delta}$

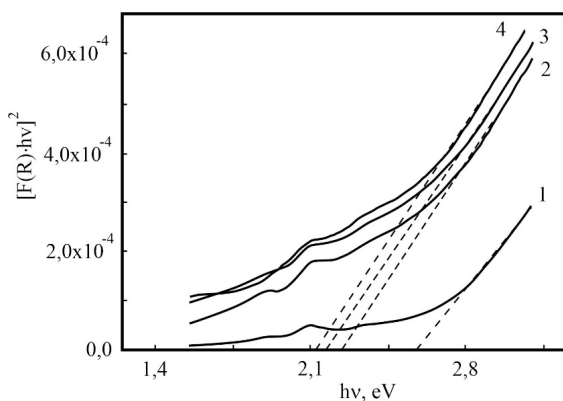


Figure 24. Diffuse reflection spectra for solid solutions $\text{La}_{1-3x}\text{Li}_x\text{M}_{2x}\text{CoO}_{3-\Delta}$: 1 – $\text{LaCoO}_{2.91}$; 2 – $\text{La}_{0.85}\text{Li}_{0.05}\text{Ca}_{0.1}\text{CoO}_{2.93}$; 3 – $\text{La}_{0.85}\text{Li}_{0.05}\text{Sr}_{0.1}\text{CoO}_{2.96}$; 4 – $\text{La}_{0.85}\text{Li}_{0.05}\text{Ba}_{0.1}\text{CoO}_{2.97}$

associated with neighboring cobalt ions and act as deep acceptor levels. As the amount of substituent x increases, the acceptor complexes interact to form σ^* -conduction band. Due to this, with some substitution on the curves of the temperature dependence of the electrical resistance, the conductivity of the samples begins to have metallic character.

Substituted cobaltates have better (comparatively to LaCoO_3) conductive properties with a slight activation barrier. An exception to the series of compounds under study is the Ba-containing complex oxide with $x = 0.1$, for which the dependence $\rho(T)$ corresponds to the typical conductivity of metals. The introduction of M^{2+} and M^+ ions may lead to the Co^{4+} ions formation (Option I: $\text{La}_{1-3x}^{3+}\text{M}_x^+\text{M}_{2x}^{2+}\text{Co}_{1-4x}^{3+}\text{Co}_{4x}^{4+}\text{O}_3$) or to the oxygen vacancies formation (option II: $\text{La}_{1-3x}^{3+}\text{M}_x^+\text{M}_{2x}^{2+}\text{Co}^{3+}\text{O}_{3-2x}$) or both at the same time. Additional thermic treatment of samples of LLBIC composition at 1153K in air for 10 hours reduces the resistivity, which probably indicates the predominance of the second variant of disorder with the formation of oxygen vacancies in cobaltates.

It is known that the semiconductor nature of conductivity can be described by several physical models. According to the standard Arrhenius law, the relationship between resistance and temperature for semiconductor systems is:

$$\rho(T) = \rho_\infty \exp(E_a/k_B T), \quad (13)$$

where ρ_∞ is the electrical resistivity at $T \rightarrow \infty$, k_B is the Boltzmann constant ($8.6 \cdot 10^{-5}$ eV/K). The value of E_a represents the band gap for the case of band conductivity of its own semiconductor or the activation energy of hopping conductivity for the case of doped semiconductor.

$$\rho(T) = \rho_\infty \exp(T_0/T)^{1/n}, \quad (14)$$

$$\ln(\rho(T)) = \ln(\rho_\infty) + (T_0/T)^{1/n} \quad (14.1)$$

$$\ln(\rho(T)) = \ln(\rho_\infty) + (T_0)^{1/n} \cdot T^{-1/n} \quad (14.2)$$

where T_0 – characteristic temperature (energy of localization of charge carriers in units of temperature). The values of $1/n = 1/4$ and $1/n = 1/3$ correspond to the three-dimensional (3D) and two-dimensional (2D) Mott hopping conductivity.

Table 11

Electrophysical characteristics of complex oxides $\text{La}_{1-3x}\text{Li}_x\text{M}_{2x}\text{CoO}_{3-8}$
(M = Ca, Sr, Ba; $0 \leq x \leq 0.1$)

Sample	$T_0, 10^5 \text{ K}$	$N(E_F), 10^{19} \text{ eV}^{-1} \cdot \text{cm}^{-3}$	$R_h, \text{ nm}$ ($T = 220\text{K}$)	$E_h, \text{ meV}$ ($T = 220\text{K}$)
LC	408	4.1	3.9	98.3
LLC1C	152	11.1	3.04	76.7
LLC2C	60	28.1	2.41	60.8
LLS1C	144	11.7	3.00	75.7
LLS2C	48	35.1	2.28	57.5
LLB1C	132	12.8	2.93	74.0
LLB2C*	-	-	-	-

*these parameters have no physical meaning, as the samples have a metallic conductivity.

Based on experimental data, the parameters characterizing the jumping conductivity were calculated. Mott characteristic temperature T_0 for hopping conductivity with variable jump length was defined as

$$T_0 = d(\ln\rho)/d(T^{-1/4}) \quad (15)$$

The density of localized states near the Fermi level $N(E_F)$ was calculated by Mott equation for the case of 3D conductivity [17]:

$$T_0 = B_0^4(\alpha^3/k_B N(E_F)), \quad (16)$$

where $\alpha = 1/a$ is the value inverse of the attenuation length of the wave function of the localized state near the Fermi level (localization length), B_0 is a constant with a value in the range of 1.7-2.5.

In cobaltates $B_0^4 = 18.108$; $a = 0.5 \text{ nm}$.

The average length R_h and jump energy E_h were calculated by the equations:

$$R_h = (3/8)a(T_0/T)^{1/4}, \quad (17)$$

$$E_h = (1/4)k_B T^{3/4} T_0^{-1/4}. \quad (18)$$

The average length of jumps of charge carriers R_h reaches the value of several interatomic distances, which is natural for the case of conductivity with variable jump length. With increasing x and size of the alkaline earth ion, there is also an increase in the density of localized states near the Fermi level, and a decrease in the average energy and jump length of charge carriers (Table 11).

Analysis of experimental dependences showed that the temperature dependence of the resistivity (Figure 25) of the samples can be described in the model of jumping conductivity with variable jump length (VRH):

$$\rho(T) = \rho_0 \exp(T_0/T)^{1/n}, \quad (19)$$

where T_0 is the Mott characteristic temperature (energy of localization of charge carriers in units of temperature); ρ_0 – preexponential factor that does not depend on temperature; $1/n = 1/4$ (the case of three-dimensional (3D) Mott hopping conductivity). Based on the above results, the calculation of the parameters of the jumping conductivity with a variable jump length: the Mott characteristic temperature T_0 and the density of localized near the Fermi level N_F states. In the simulation, we used the Mott ratio for the characteristic temperature at 3D conductivity.

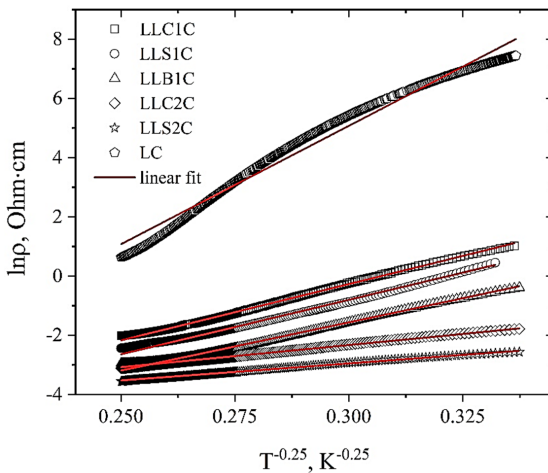


Figure 25. Processing of experimental dependences $\ln \rho$ in coordinates corresponding to the three dimensional Mott conductivity for $\text{La}_{1-3x}\text{Li}_x\text{M}_{2x}\text{CoO}_{3-\Delta}$ ($M = \text{Ca, Sr, Ba}$; $0 \leq x \leq 0.1$) system.

Reducing the characteristic temperature of the hopping conductivity, increasing the density of localized states and defects in the structure, increases the electrical conductivity of lanthanum cobaltate, doped simultaneously by alkaline earth metals ions and lithium.

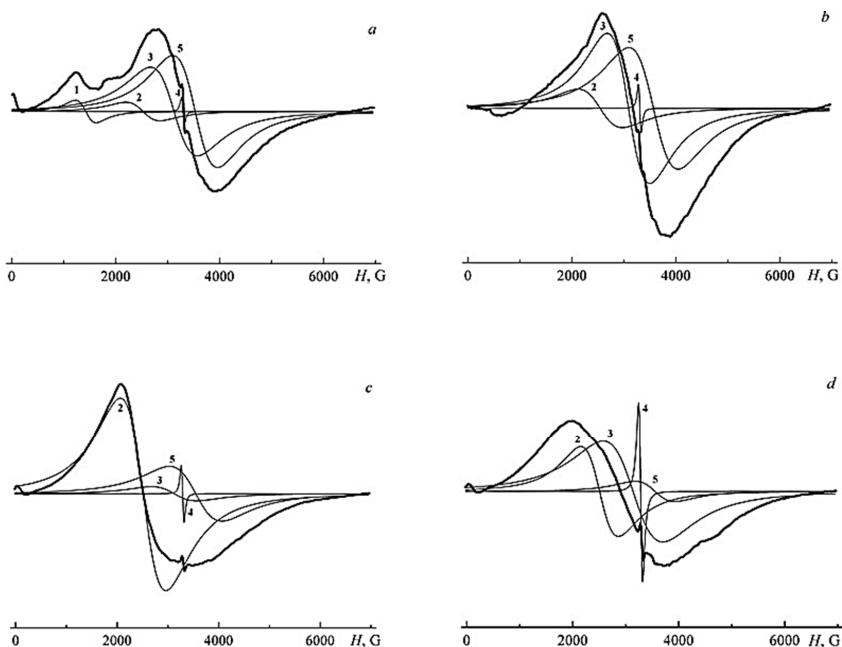


Figure 26. EPR spectra of starting $\text{LaCoO}_{3-\Delta}$ (a) and $\text{La}_{0.85}\text{Li}_{0.05}\text{M}_{0.1}\text{CoO}_{3-\Delta}$ [$\text{M} = \text{Ca}$ (b), Sr (c), Ba (d)] at room temperature

Figure 26 shows the EPR spectra of the studied samples, which are a superposition of five (undoped LaCoO_3) and four (doped LaCoO_3) Lorentzian-shaped lines (the simulation was carried out with an accuracy of 99%). This indicates the presence of several defect centers in the structure. When the resonance line is decomposed into components, the values of g -factors, line widths ΔH and areas under the absorption curves (integral intensities) were obtained for each line. In the case of pure LaCoO_3 , it was possible to record the signal (1) with $g_{\text{eff}} = 5.00$ and $\Delta H = 680$ G from isolated Co^{2+} ions – structural defect centers in the perovskite matrix. This is fully consistent with the results of iodometric titration. Indeed, $\text{LaCoO}_{3-\Delta}$ ($\Delta = 0.09$) is a compound that is non-stoichiometric in oxygen. The emergence of oxygen vacancies is accompanied by a decrease in the formal

oxidation state ($\text{Co}^{n+} = 2.95$) of some of the structural ions $\text{Co}^{3+} \rightarrow \text{Co}^{2+}$, which retain the octahedral oxygen environment.

In strontium-containing samples, there are mainly ferromagnetic clusters $\text{Co}^{3+}\text{-Co}^{4+}$ in the form of spin heptamers $(\text{Co}^{3+})_6\text{Co}^{4+}$, which correspond to band (2) with $g_{\text{eff.}} = 2.80$ and $\Delta H = 1100 - 1500$ G. In the case of substitution of La by (Ba, Li) and (Ca, Li), the ferromagnetic interaction of Co^{4+} and Co^{3+} ions do not allow the clusters to group into larger agglomerates compared to cobaltate containing Sr.

The characteristics of the signal (3) ($g_{\text{eff.}} = 2.25$ and $\Delta H \approx 1500$ G) provide grounds for identifying paramagnetic Co^{2+} ions in the form of a Co_3O_4 impurity, which is formed as a result of the thermolysis of the precursor. It has been established that Co^{2+} ions are in different local environments and have different degrees of exchange interaction with each other, contained in the form of chain fragments $\text{-Co}^{2+}\text{-O}^{2-}\text{-Co}^{2+}\text{-O}^{2-}\text{-Co}^{2+}\text{-O}^{2-}$ (Figure 27). It is also worth noting that the presence of the Co_3O_4 phase in the cobaltate matrices could not be detected by the X-ray diffraction method, while the sensitivity of the EPR method turned out to be sufficient for detecting weakly interacting Co^{2+} ions.

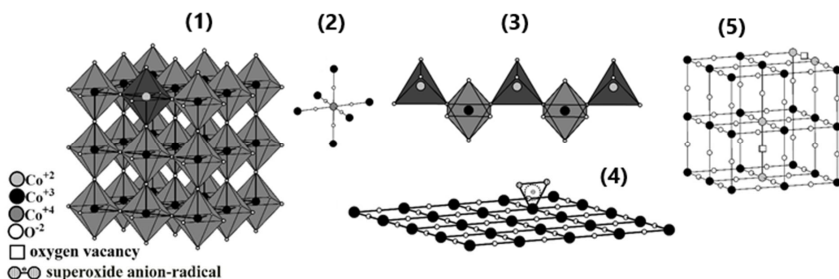


Figure 27. Schematic illustration of the defect centers on the LaCoO_3 : Li^+ ; M^{2+} ($\text{M} = \text{Ca}, \text{Sr}, \text{Ba}$) surface according to the EPR spectroscopy data

A characteristic feature of the synthesized lanthanum cobaltates with a perovskite structure is the appearance in the EPR spectra of a narrow line (4) with $g_{\text{eff.}} = 2.14$ and $\Delta H \approx 40$ G, which is due to the formation of surface

complexes of the superoxide anion radical $O_2^{\cdot-}$ with Co^{3+} ions – $[Co^{3+}\cdots O_2^{\cdot-}]$. The formation of such an adduct can occur during the sorption of molecular oxygen on the surface of the oxide matrix containing defective Co^{2+} centers. The concentration of paramagnetic fragments $[Co^{3+}\cdots O_2^{\cdot-}]$ in the studied samples reaches a value of the order of 10^{15} g^{-1} . It should also be noted the extremely high stability of the indicated cobalt-oxygen complexes: the concentration of paramagnetic particles in the composition of the samples of doped lanthanum cobaltates after two years of storage in air practically did not change. The largest contribution of a signal of this nature was recorded for Ba-containing cobaltate, which is probably due to the stabilization of the surface defect by cations with a large ionic radius.

Line (5) in the EPR spectrum with $g_{eff.} = 2.02$ and $\Delta H \approx 1600 - 1700 \text{ G}$ is due to defect centers of Co^{2+} , which are formed during the desorption of lattice oxygen from the surface, or during the diffusion of oxygen from the bulk of the material to the surface.

Figures 28-29 shows the measurement of the diffuse reflectance of prepared lanthanum orthoferrites. As a rule, the electronic configuration of La ($4f^1$) significantly affects the optical properties of ferrites.

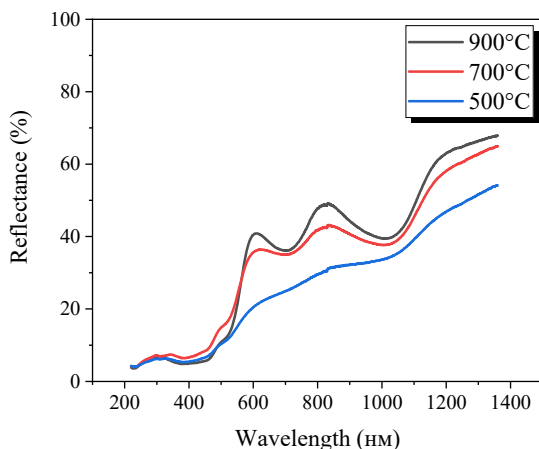


Figure 28. Diffuse reflectance spectra of $LaFeO_3$ synthesized using citrate method at different temperatures

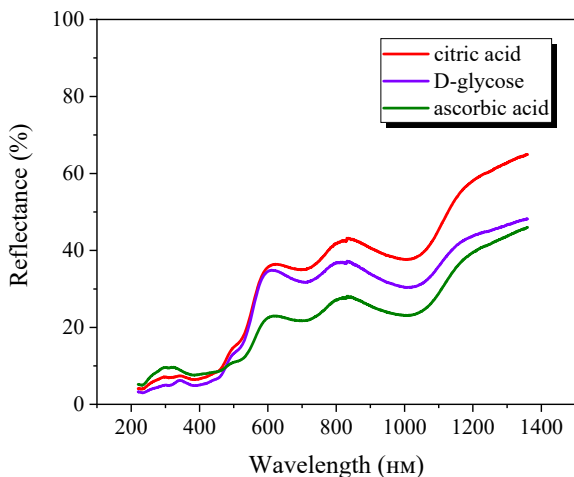


Figure 29. Diffuse reflectance spectra of LaFeO_3 synthesized using various complexing agents (chelating agents)

All samples show a minimum reflection spectrum in the wavelength range from 200 to about 400 nm. This is followed by a high increase in the reflectance near the UV edge.

It turns out that lanthanide ions can be excited in three different ways, so three excitation transitions can be distinguished: internal 4f transitions (4f-4f), 4f-5d transitions and charge transfer transitions.

In 4f-5d transitions, the 4f electron can be excited to a higher energy orbital, which is the 5d orbital. This type of transition is usually denoted as $4f^n-4f^{n-1} 5d$ and is usually observed for Ce^{3+} , which has an electronic configuration of $4f^1$. Moreover, the excess 4f electrons in Ce^{3+} can be easily transferred to the 5d orbital. Their broad reflection bands arise from configurational transitions, for example, from 4 to $4f^{n-1} 5d$.

On the other hand, in charge transfer transitions (CTTs), 2p electrons from neighboring anions (e.g., O^{2-} in oxides) can be transferred to the 4f orbital of La^{3+} ions. This type of transition can be observed in Sm^{3+} , which has an electronic configuration of $4f^5$ and requires additional electrons for stability. Such transitions are allowed and exhibit intense and broad reflection bands.

Figure 28 shows the diffuse reflectance spectra in the UV and visible regions of the spectrum for LaFeO₃ particles synthesized at different temperatures. It can be seen that with increasing synthesis temperature, the reflection of visible light by LaFeO₃ particles increases.

The bandgap energies of the samples can be obtained from the corresponding first derivative spectra, where the peak wavelengths are characterized by the absorption edges of the samples. For LaFeO₃ particles, two absorption bands are observed at 476-480 and 548-562 nm, which are explained by the charge transfer from the ligand to the metal Fe³⁺ (LMCT) and the excitation of two neighboring high-spin Fe³⁺ centers (i.e., metal-to-metal charge transfer, MMCT), respectively.

Table 12

The positions of the absorption bands and the corresponding transition energies for the electronic spectrum of LaFeO₃ synthesized at different temperatures and using different chelating agents

λ_{LMCT} , nm	λ_{MMCT} , nm	E_{LMCT} , eV	E_{MMCT} , eV	Sample
476	548	2.60	2.26	LaFO_500_CA
478	556	2.59	2.22	LaFO_700_CA
480	562	2.58	2.20	LaFO_900_CA
478	557	2.59	2.22	LaFO_700_G
477	562	2.60	2.20	LaFO_700_AA

From the absorption edges, two bandgap energies of LaFeO₃ particles were obtained (Table 12): 2.58-2.60 and 2.20-2.26 eV depending on the sample processing temperature. With increasing annealing temperature, the bandgap width of lanthanum ferrite decreases slightly. On the other hand, when using different types of fuel, both absorption edges of LaFeO₃ particles almost do not shift, which means a slight change in their bandgap energies. Such small bandgap values of LaFeO₃ are interesting for applications in photocatalytic, sensor materials, and electrode materials in solid oxide fuel cells (SOFCs).

Conclusions

Solid solutions of La_{0.8-x}Na_xMn_{0.2}O_{1+x-3Δ} (0 ≤ x ≤ 0.2) were synthesized by the sol-gel autocombustion method. It was found that as a result of the

thermally induced redox reaction that occurs in the nitrate-citrate gel, a sufficient amount of energy is released to form single-phase perovskites at fairly low temperatures, even at 500 °C.

With increasing temperature of synthesis of samples, a decrease in the parameters of the crystal cell (a , c) and the volume of the unit cell V was recorded, which may be a consequence of the process of thermally induced ordering of ions and/or vacancies of the cationic and/or anionic sublattice, while the average values of the coherent scattering regions and the degree of crystallinity increase. The X-ray density for manganite nanopowders, calculated from powder diffraction data, and the Mn-O-Mn angle increase directly proportional to the temperature of isothermal treatment, while the Mn-O distance decreases. This fact may also indicate a decrease in the defectivity of the perovskite structure and a simultaneous increase in the 2p-3d hybridization between O and Mn ions, the exchange interaction between Mn-Mn ions during the heat treatment process.

It was found that the region of existence of solid solutions $\text{La}_{0.8-x}\square_x\text{Na}_{0.2}\text{Mn}_{1+x}\text{O}_{3-\Delta}$ is limited to the composition $x=0.1$. With an increase in the overstoichiometric manganese content and the concentration of cation vacancies in the A-position, the impurity phase Mn_3O_4 is formed, and the lattice parameters of the main perovskite phase decrease, which indicates the appearance of Mn_A^{2+} . The appearance of Mn^{2+} ions, which occupy the A-position together with larger La^{3+} and Na^+ ions, leads to a distortion of the perovskite structure. Based on the experimental data, it can be predicted that an increase in the Mn-O bond length and a decrease in the Mn-O-Mn angle will favorably affect the magnetotransport properties of manganites.

With the simultaneous substitution of triple-charged lanthanum for double-charged strontium and the introduction of overstoichiometric manganese in the B-position, it was possible to obtain single-phase manganite $\text{La}_{0.6}\text{Sr}_{0.3}\text{Mn}_{1.1}\text{O}_3$, the crystal structure of which was established for the first time.

Using the X-ray diffraction method, it is shown that the appearance of non-stoichiometric manganese in the composition of substituted manganite leads to charge disorder in the perovskite structure, and the real defect structure contains ions of different valences Mn_B^{4+} , Mn_B^{3+} , Mn_A^{2+} , as well as cationic $V^{(c)}$ and anionic $V^{(a)}$ vacancies. It is established that with heterovalent

substitution of lanthanum by singly and/or doubly charged ions, there is a decrease in the parameters of the crystal lattice and the volume of the unit cell, despite the larger ionic radii of the substituents compared to lanthanum. This pattern may be due to the appearance of a compensating defect Mn^{4+} (0.53 Å) with a much smaller ionic radius than Mn^{3+} (0.645 Å), which mainly exists in the structure of unsubstituted lanthanum manganite.

Using EPR spectroscopy, paramagnetic defect centers containing Co^{2+} ions and ferromagnetic Co^{3+} - Co^{4+} clusters were detected on the surface of the oxide matrix. For the first time, surface complexes $[Co^{3+}\cdots O_2^-]$ were identified for the perovskite system, the concentration of which increases with increasing ionic radius of the modifying additive. Based on the results obtained, it was suggested that these fragments play the role of catalytically active centers, and the possibility of using synthesized lanthanum cobaltates as catalysts was predicted.

Addition of Ca, Sr, Ba, and Li dopants to $LaCoO_3$ was shown to increase the optical band gap whereas the specific electrical resistance decreased.

References:

1. Bochenek D., Niemiec P., Skulski R., Adamczyk-Habrajska M. (2019). Electrophysical properties of a multicomponent PZT-type ceramics for actuator applications. *Journal of Physics and Chemistry of Solids*, 133, 128-134. DOI: <https://doi.org/10.1016/j.jpcs.2019.05.015>
2. Selmani Y., Mouatassime M., Goumrhar F., Labrim H., Bahmad L., Benyoussef A. (2021). Structural, electronic and magnetic properties of the perovskite $YMnO_3$. *Solid State Communications*, 328, 114254. DOI: <https://doi.org/10.1016/j.ssc.2021.114254>
3. Elganich H., Elrhazouani O., Halimi A., Mkimel M., Ait Ahmed Y., Saad E. (2021). Magnetic properties of the perovskite $GdCuO_3$: Monte Carlo simulation. *Physics Letters A*, 412, 127587. DOI: <https://doi.org/10.1016/j.physleta.2021.127587>
4. Xi Xuan, Cao Zeng-Sheng, Shen Xin-Quan, Lu Ying, Li Jun, Luo Jing-Li, Fu Xian-Zhu. (2020). *In situ* embedding of CoFe nanocatalysts into Sr_2FeMoO_7 matrix as high-performance anode materials for solid oxide fuel cells. *Journal of Power Sources*, 459, 228071. DOI: <https://doi.org/10.1016/j.jpowsour.2020.228071>
5. Zhang C., Hen H., Wang N., Chen H., Kong D. (2013). Visible-light sensitive $La_{1-x}Ba_xCoO_3$ photocatalyst for malachite green degradation. *Ceramics International*, 39(4), 3685-3689. DOI: <https://doi.org/10.1016/j.ceramint.2012.10.200>
6. Dong B., Li Z., Li Z., Xu X., Song M., Zheng W., Wang C., Al-Deyab S. S., El-Newehy M. (2010). Highly Efficient $LaCoO_3$ Nanofibers Catalysts for Photocatalytic Degradation of Rhodamine B. *Journal of the*

American Ceramic Society, 93(11), 3587-3590. DOI: <https://doi.org/10.1111/j.1551-2916.2010.04124.x>

7. Su D., Liedienov N.A., Kalita V.M., Fesych I.V., Xu W., Bodnaruk A.V., Dzhzherya Yu.I., Li Q., Liu B., Levchenko G.G. (2024). Structural size effect-, aging time-, and pressure-dependent functional properties of Mn-containing perovskite nanoparticles. *Acta Materialia*, 280, 120332. DOI: <https://doi.org/10.1016/j.actamat.2024.120332>

8. Franco V., Blazquez J.S., Ipus J.J., Law J.Y., Moreno-Ramirez L.M., Conde A. (2018). Magnetocaloric effect: From materials research to refrigeration devices. *Progress in Materials Science*, 93, 112-232. DOI: <https://doi.org/10.1016/j.pmatsci.2017.10.005>

9. Gschneidner Jr K.A., Pecharsky V.K., Tsokol A.O. (2005). Recent developments in magnetocaloric materials. *Reports on Progress in Physics*, 68(6), 1479-1539. DOI: <https://doi.org/10.1088/0034-4885/68/6/R04>

10. Arun B., Akshay V.R., Mutta G.R., Venkatesh C., Vasundhara M. (2017). Mixed rare earth oxides derived from monazite sand as an inexpensive precursor material for room temperature magnetic refrigeration applications. *Materials Research Bulletin*, 94, 537-543. DOI: <https://doi.org/10.1016/j.materresbull.2017.07.006>

11. Wali M., Skini R., Khelifi M., Dhahri E., Hlil E.K. (2015). Effect of the oxygen deficiency on the physical properties of $\text{La}_{0.8}\text{Na}_{0.2}\text{MnO}_{3-\delta}$ oxides ($\delta = 0$ and 0.05). *Journal of Magnetism and Magnetic Materials*, 394, 207-211. DOI: <https://doi.org/10.1016/j.jmmm.2015.06.042>

12. Abou-Ras D., Boujelben W., Cheikh-Rouhou A., Pierre J., Renard J.P., Reversat L., Shimizu K. (2001). Effect of strontium deficiency on the transport and magnetic properties of $\text{Pr}_{0.7}\text{Sr}_{0.3}\text{MnO}_3$. *Journal of Magnetism and Magnetic Materials*, 233(3), 147-154. DOI: [https://doi.org/10.1016/S0304-8853\(01\)00273-6](https://doi.org/10.1016/S0304-8853(01)00273-6)

13. Arun B., Akshay V.R., Vasundhara M. (2018). Observation of enhanced magnetocaloric properties with A-site deficiency in $\text{La}_{0.67}\text{Sr}_{0.33}\text{MnO}_3$ manganite. *Dalton Transactions*, 47(43), 15512-15522. DOI: <https://doi.org/10.1039/C8DT03538E>

14. Pashchenko A.V., Pashchenko V.P., Prokopenko V.K., Revenko Y.F., Prylipko Y.S., Ledenev N.A., Levchenko G.G., Dyakonov V.P., Szymczak H. (2014). Influence of structure defects on functional properties of magnetoresistance ($\text{Nd}_{0.7}\text{Sr}_{0.3-x}\text{Mn}_{1+x}\text{O}_3$) ceramics. *Acta Materialia*, 70, 218-227. DOI: <https://doi.org/10.1016/j.actamat.2014.02.014>

15. Pashchenko A.V., Pashchenko V.P., Prokopenko V.K., Revenko Y.F., Mazur A.S., Burchovetskii V.V., Turchenko V.A., Liedienov N.A., Pitsyuga V.G., Levchenko G.G., Dyakonov V.P., Szymczak H. (2016). The role of structural and magnetic inhomogeneities in the formation of magneto-transport properties of the $\text{La}_{0.6-x}\text{Sm}\text{Sr}_{0.3}\text{Mn}_{1-x}\text{O}_{3-\delta}$ ceramics. *Journal of Magnetism and Magnetic Materials*, 416, 457-465. DOI: <https://doi.org/10.1016/j.jmmm.2016.05.010>

16. Orgiani P., Aruta C., Ciancio R., Galdi A., Maritato L. (2013). Synthesis and properties of highly metallic orbital-ordered A-site manganites. *Journal*

of *Nanoparticle Research*, 15(6), 1655(1-9). DOI: <https://doi.org/10.1007/s11051-013-1655-9>

17. AboZied A.E.-R.T., Ghani A.A., Ali A.I., Salaheldin T.A. (2019). Structure, magnetic and magnetocaloric properties of nano crystalline perovskite $\text{La}_{0.8}\text{Ag}_{0.2}\text{MnO}_3$. *Journal of Magnetism and Magnetic Materials*, 479, 260-267. DOI: <https://doi.org/10.1016/j.jmmm.2019.02.043>

18. Kriener M., Braden M., Kierspel H., Senff D., Zabara O., Zobel C., Lorenz T. (2009). Magnetic and structural transitions in $\text{La}_{1-x}\text{A}_x\text{CoO}_3$ (A = Ca, Sr, and Ba). *Physical Review B*, 79(22), 224104. DOI: <https://doi.org/10.1103/PhysRevB.79.224104>

19. Plakhty V.P., Brown P.J., Grenier B., Shiryayev S.V., Barilo S.V., Gavrilov S.V., Ressouche E. (2006). Thermal excitation of the Co^{3+} triplet spin-state in LaCoO_3 determined by polarized neutron diffraction. *Journal of Physics: Condensed Matter*, 18(13), 3517-3525. DOI: <https://doi.org/10.1088/0953-8984/18/13/019>

20. Podlesnyak A., Conder K., Pomjakushina E., Mirmelstein A., Allenspach P., Khomskii D.I. (2007). Effect of light Sr doping on the spin-state transition in LaCoO_3 . *Journal of Magnetism and Magnetic Materials*, 310(2), 1552-1554. DOI: <https://doi.org/10.1016/j.jmmm.2006.10.901>

21. Humayun M., Ullah H., Usman M., Habibi-Yangjeh A., Ali Tahir A., Wang C., Luo W. (2021). Perovskite-type lanthanum ferrite based photocatalysts: Preparation, properties, and applications. *Journal of Energy Chemistry*, 66, 314-338. DOI: <https://doi.org/10.1016/j.jechem.2021.08.023>

22. Varma A., Mukasyan A.S., Rogachev A.S. and Manukyan K.V. (2016). Solution Combustion Synthesis of Nanoscale Materials. *Chemical Reviews*, 116(23), 14493-14586. DOI: <https://doi.org/10.1021/acs.chemrev.6b00279>

23. Xu G., Ma H., Zhong M., Zhou J., Yue Y., He Z. (2006). Influence of pH on characteristics of $\text{BaFe}_{12}\text{O}_{19}$ powder prepared by sol-gel auto-combustion. *Journal of Magnetism and Magnetic Materials*, 301(2), 383-388. DOI: <https://doi.org/10.1016/j.jmmm.2005.07.014>

24. Scherrer P. (1918). Bestimmung der Größe und der inneren Struktur von Kolloidteilchen mittels Röntgenstrahlen. *Nachrichten von der Gesellschaft der Wissenschaften zu Göttingen, Mathematisch-Physikalische Klasse*, 2, 98-100.

25. Langford J. and Wilson A. (1978). Scherrer after sixty years: a survey and some new results in the determination of crystallite size. *Journal of Applied Crystallography*, 11(2), 102-113. DOI: <https://doi.org/10.1107/S0021889878012844>

26. Dhaouadi H., Ghodbane O., Hosni F., Touati F. (2012). Mn_3O_4 Nanoparticles: Synthesis, Characterization, and Dielectric Properties. *International Scholarly Research Notices*, 2012, 1-8. DOI: <https://doi.org/10.5402/2012/706398>

27. Ianculescu A., Braileanu A., Zaharescu M., Pasuk I., Chirtop E., Popescu C., Segal E. (2001). Phase Formation Study of The Substituted Lanthanum Manganites Solid Solutions. *Journal of Thermal Analysis and Calorimetry*, 64(3), 1001-1010. DOI: <https://doi.org/10.1023/A:1011539400575>

28. Wei Z., Pashchenko A.V., Liedienov N.A., Zatovsky I.V., Butenko D.S., Li Quanjun, Fesych I.V., Turchenko V.A., Zubov E.E., Polynchuk P.Yu., Pogrebnyak V.G., Poroshin V.M. and Levchenko G.G. (2020). Multifunctionality

of lanthanum–strontium manganite nanopowder. *Physical Chemistry Chemical Physics*, 22(21), 11817-11828. DOI: <https://doi.org/10.1039/D0CP01426E>

29. Shannon R.D. (1976). Revised Effective Ionic Radii and Systematic Studies of Interatomic Distances in Halides and Chalcogenides. *Acta Crystallographica*, A32, 751-767. DOI: <https://doi.org/10.1107/S05677394760001551>

30. Evdou A., Georgitsis T., Matsouka C., Pachatouridou E., Iliopoulou E., Zaspalis V. (2022). Defect Chemistry and Chemical Looping Performance of $\text{La}_{1-x}\text{M}_x\text{MnO}_3$ (M = Sr, Ca, (x = 0-0.5)) Perovskites. *Nanomaterials*, 12(19), 3461. DOI: <https://doi.org/10.3390/nano12193461>

31. Pashchenko A.V., Pashchenko V.P., Liedienov N.A., Prokopenko V.K., Revenko Yu.F., Pismenova N.E., Burhovetskii V.V., Sycheva V.Y., Voznyak A.V., Levchenko G.G., Dyakonov V.P., Szymczak H. (2017). Structure, phase transitions, ^{55}Mn NMR, magnetic and magnetotransport properties of the magnetoresistance $\text{La}_{0.9-x}\text{Ag}_x\text{Mn}_{1.1-3x}\text{O}_{3-\delta}$ ceramics. *Journal of Alloys and Compounds*, 709, 779-788. DOI: <https://doi.org/10.1016/j.jallcom.2017.03.093>

32. Medarde M., Mesot J., Lacorre P., Rosenkranz S., Fischer P., and Gobrecht K. (1995). High-pressure neutron-diffraction study of the metallization process in PrNiO_3 . *Physical Review B*, 52, 9248. DOI: <https://doi.org/10.1103/PhysRevB.52.9248>

33. Pashchenko A.V., Liedienov N.A., Fesych I.V., Li Q., Pitsyuga V.G., Turchenko V.A., Pogrebnyak V.G., Liu B., Levchenko G.G. (2020). Smart magnetic nanopowder based on the manganite perovskite for local hyperthermia. *RSC Advances*, 10(51), 30907-30916. DOI: <https://doi.org/10.1039/d0ra06779b>

34. Liedienov N.A., Kalita V.M., Pashchenko A.V., Dzhzherya Yu.I., Fesych I.V., Li Q., Levchenko, G.G. (2020). Critical phenomena of magnetization, magnetocaloric effect, and superparamagnetism in nanoparticles of non-stoichiometric manganite. *Journal of Alloys and Compounds*, 836, 155440(1-11). DOI: <https://doi.org/10.1016/j.jallcom.2020.155440>

35. Dzhzherya Y.I., Xu W., Cherepov S.V., Skirta Y.B., Kalita V.M., Bodnaruk A.V., Liedienov N.A., Pashchenko A.V., Fesych I.V., Liu B., Levchenko G.G. (2021). Magnetoactive elastomer based on superparamagnetic nanoparticles with Curie point close to room temperature. *Materials and Design*, 197, 109281(1-8). DOI: <https://doi.org/10.1016/j.matdes.2020.109281>